

DESIGN, FABRICATION, AND CHARACTERIZATION OF A MICROMACHINED HEAT
EXCHANGER PLATFORM FOR THERMOELECTRIC POWER GENERATION

By

SIVARAMAN MASILAMANI

A THESIS PRESENTED TO THE GRADUATE SCHOOL
OF THE UNIVERSITY OF FLORIDA IN PARTIAL FULFILLMENT
OF THE REQUIREMENTS FOR THE DEGREE OF
MASTER OF SCIENCE

UNIVERSITY OF FLORIDA

2008

© 2008 Sivaraman Masilamani

To my mother, Chitra Masilamani, and
to the memory of my father, Masilamani Sambandhamoorthy

ACKNOWLEDGMENTS

I would like to express my deepest thanks and gratitude to my advisor, Dr. David Arnold for the invaluable opportunities, career and personal advice, and for his compassion during the most difficult times. Without his endless patience, persistent motivation and continued appreciation for hard work, this research work would have not been possible. I also extend my sincere thanks to Dr. Toshikazu Nishida and Dr. David Hahn for serving on my thesis committee. I am also grateful to Army Research Laboratories for the financial support they provided for this research.

I would like to cordially thank my project colleagues Israel Boniche, Christopher Meyer, and Eric Viale for their insight and assistance during the course of this research. Special thanks go to Ryan Durscher for his help with device modeling and for the many weekends he assisted me in the laboratory. Several other IMG-ers have been of genuine help to me during my graduate study. In particular, I would like to thank Janhavi Agashe, for her cheerful encouragement, academic and personal advice, Sheetal Shetye, for her friendly guidance and cleanroom help, Erin Patrick, for help with the microdispenser, Mingliang Wang and Yawei Li for their valuable microfabrication insights. I also acknowledge Al Ogden for his help with cleanroom equipment. I also owe special thanks to my undergraduate friends that lived with me in Bangalore, for their encouragement and support.

Finally, I would like to thank my parents, Masilamani Sambandhamoorthy and Chitra Masilamani, for their uncountable love and support all my life. The great human values, work ethics, and perseverance that they inculcated in me are the reasons behind everything that I achieve. I also thank my brother, Raghuraman Masilamani, for his care and affection. Last but not least, I thank my fiancée, Gayathri Devi Sridharan, for giving me the strength to face challenges; and for her fondness and love.

TABLE OF CONTENTS

	<u>page</u>
ACKNOWLEDGMENTS	4
LIST OF TABLES	7
LIST OF FIGURES	8
ABSTRACT	10
CHAPTER	
1 INTRODUCTION AND BACKGROUND	12
1.1 Heat Exchangers.....	13
1.2 MEMS Heat Exchangers and Applications	15
1.3 Thermoelectric Power Generation	18
1.3.1 Seebeck Effect.....	19
1.3.2 Peltier Effect	19
1.3.3 Thomson Effect.....	20
1.3.4 Thermoelectric Generator	20
1.4 Microscale TE Generators.....	22
1.5 Research Goals.....	25
1.6 Thesis Outline	25
2 HEAT EXCHANGER DEVICE DESIGN AND MODELING.....	27
2.1 Thermopile Material and Arrangement.....	28
2.2 Structure of Thermoelectric Microgenerator	29
2.2.1 Simple in-Plane TEG Structure.....	34
2.2.2 Out-of-Plane Flip-Chip Bonded Structure	35
2.2.3 Vertically Stacked Thermopile Structure.....	37
2.2.4 Vertically Stacked Radial In-plane Structure.....	38
2.3 Device Design	40
2.3.1 Fin Geometry Optimization	42
2.3.2 Exhaust Gas Channel Design.....	45
2.3.3 Ring Thickness and Space between Rings.....	46
2.4 Thermal Modeling.....	48
2.5 Final Dimensions of the Radial In-plane TE Modules.....	52
2.6 Summary	52
3 FABRICATION AND STACKING OF THE HEAT EXCHANGER MODULES	53
3.1 Through-Etching of Wafers	53
3.2 Membrane Strength Evaluation.....	54
3.3 Process Flow Description.....	55

3.4	Mask Making	56
3.5	Stacking and Bonding of Heat Exchanger Unit Modules	58
3.6	Final Device Photographs	61
3.7	Summary	61
4	CHARACTERIZATION OF THE HEAT EXCHANGER DEVICE	62
4.1	Experimental Setup and Procedure	62
4.1.1	Flow Measurements	64
4.1.2	Temperature Measurements	67
4.2	Test Matrix and Actual Test Results	69
4.3	Comparison with Predicted Results	75
4.4	Limitations of the Experimental Setup	77
4.5	Summary	78
5	CONCLUSIONS AND FUTURE WORK	79
5.1	Conclusions	79
5.2	Future Work	80
5.2.1	Eutectic Bonding of TE Modules	81
5.2.2	Integrated Temperature Measurement	82
	LIST OF REFERENCES	85
	BIOGRAPHICAL SKETCH	89

LIST OF TABLES

<u>Table</u>		<u>page</u>
1-1	Heat exchanger classification	14
3-1	Heat exchanger process flow	56
4-1	Flow velocity measurement procedure using the CTA.....	66
4-2	Heat exchanger characterization matrix.....	70
4-3	Temperatures measured during heat exchanger characterization	70

LIST OF FIGURES

<u>Figure</u>		<u>page</u>
1-1	Common example of a heat exchanger.....	13
1-2	Extended surface heat exchanger used in electronic cooling.....	14
1-3	Different fin configurations	15
1-4	Compact heat sink implemented by Tuckerman and Pease.....	16
1-5	Improved MEMS electronic cooling methods.....	16
1-6	Micro heat exchangers for heat engines.....	17
1-7	Thermoelectric effect.....	19
1-8	Basic thermoelectric generator	21
1-9	TE generator with integrated heat exchangers.....	22
1-10	Examples of micro TEGs.....	24
1-11	Concept of thermoelectric cooling.....	24
2-1	Thin-film TEG	28
2-2	Planar TEG structure.....	30
2-3	In-plane TEG	35
2-4	Out-of-plane TEG with top Si plate removed.....	36
2-5	Thermopile formation in out-of-plane TEG	37
2-6	Vertically stacked thermopile structure	38
2-7	Stacked radial in-plane structure.....	39
2-8	First-order equivalent thermal circuit of a radial in-plane TE module	40
2-9	Dimensions of a single radial thermocouple leg.....	41
2-10	Fin geometry optimization.....	44
2-11	Detailed thermal model of radial in-plane structure	48
2-12	Final device dimensions.....	52

3-1	Heat exchanger module to be fabricated.....	54
3-2	Device cross-sections during various process steps.....	57
3-3	Mask patterns.....	58
3-4	Assembly jig.....	59
3-5	Epoxies for bonding heat exchanger modules.....	60
3-6	Epoxy application methods.....	60
3-7	Heat exchanger stack built with square shaped modules.....	61
3-8	Heat exchanger built with circular modules.....	61
4-1	Experimental setup to test the heat exchanger device.....	62
4-2	Heat exchanger device bonded with the fluidic coupler.....	63
4-3	System schematic of a constant temperature anemometer.....	64
4-4	Temperature measurement tools.....	67
4-5	Device temperature measurement points.....	68
4-6	Variation of inner and outer ring temperatures with increasing hot-air temperature.....	71
4-7	Variation in inner silicon ring temperature with hot-air velocity.....	74
4-8	Comparison of experimental results with results predicted by analytical model.....	76
5-1	Eutectic bonding of TE modules.....	81
5-2	Top view of the TE module with integrated RTDs.....	83

Abstract of Thesis Presented to the Graduate School
of the University of Florida in Partial Fulfillment of the
Requirements for the Degree of Master of Science

DESIGN, FABRICATION, AND CHARACTERIZATION OF A MICROMACHINED HEAT
EXCHANGER PLATFORM FOR THERMOELECTRIC POWER GENERATION

By

Sivaraman Masilamani

August 2008

Chair: David Arnold

Major: Electrical and Computer Engineering

The ever-continuing trend in miniaturization and ever-growing power density requirement of portable electronics has necessitated the search for alternate sources of compact power with high energy content. To this end, new technologies such as microscale heat engines, micro fuel cells, micro-thermo photovoltaic and micro-thermoelectric generation are being developed as possible alternatives to traditional battery technologies. Among these, thermoelectric generators boast many key advantages such as robustness, reliability and long-life. Thermoelectrics devices enable the direct conversion of heat energy into electrical energy.

Recent advancements in thermoelectric materials and increased demand for power in the microwatt to milliwatt range have fueled wider research on microscale thermoelectric generators. Traditionally, when scaled down, these generators suffer from fairly large thermal leakage; it is difficult to maintain a large temperature differential because of the small physical dimensions. This thesis presents the design, fabrication and characterization of a heat exchanger platform for thermoelectric power generation using waste heat from a small combustion engine while attempting to mitigate the thermal leakage problem.

After evaluating several different heat exchanger device structures based on the desired performance parameters, a stacked radial in-plane structure was chosen. The design consists of

several heat exchanger modules stacked vertically to form a tubular structure. Each module has two concentric silicon rings connected only by a 5 μm thin supporting membrane to achieve low thermal leakage. This design offers an ideal compromise between thermal leakage, mechanical robustness and fabrication complexity.

An analytical model of the device was built to predict the device performance, and a process flow was developed to fabricate the proposed radial in-plane heat exchanger. With a simple two mask process, devices were fabricated using planar microfabrication and bulk-micromachining techniques. Heat exchanger devices were then characterized in the laboratory under varied test conditions. The experimentally obtained data was found to agree well with analytically predicted performance.

In conclusion, the contributions of this research work are twofold. First, it proves the feasibility of a mechanically robust radial in-plane heat exchanger structure for thermoelectric power generation from hot exhaust gasses. Second, it demonstrates the possibility of achieving low thermal leakage in an appropriately designed, $\sim 1 \text{ cm}^3$ device.

CHAPTER 1 INTRODUCTION AND BACKGROUND

The recent boom in the wireless communications industry and the continuing trend in miniaturization of portable electronics have placed a large and expanding demand for portable power sources. Batteries, in spite of their latest advancements, fall short to meet the rising energy densities asked of them. Attention has, therefore, turned to other sources of high energy content such as hydrocarbon and alcohol fuels. This paradigm shift in the portable power industry has provided the impetus to the development of many new technologies.

Some of the common approaches adopted to exploit the high specific energy of hydrocarbon fuels are miniaturization of existing large scale systems such as gas turbines and internal combustion engines, direct energy conversion schemes such as thermo photovoltaic and thermoelectric generation, and fuel cells. The remarkable advancement in MEMS technology over the years has enabled pursuit of successful research in each of these areas.

The focus of this research is thermoelectric (TE) power generation. Bulk TE generators have been in usage for more than half-a-century in many niche applications, yet only recently thin thermoelectric materials with reasonable efficiency, suitable for microscale integration were available [1]. Following this, a host of research initiatives were launched, aiming at different applications of microscale TE power generation – either as stand alone compact power sources or as a part of a system such as microscale heat engine, to improve the overall efficiency.

For a microscale TE generator to achieve best performance, a high temperature difference needs to be created across a very short distance in the range of hundreds of micrometers. Depending on the application, heat exchangers can be integrated with the generator to improve the temperature difference. The aim of this work is to design and fabricate a heat exchanger

platform that can extract heat energy from the exhaust gas of an internal combustion engine, and develop the temperature differential required for a TE microgenerator.

1.1 Heat Exchangers

A heat exchanger may be defined as a device that enables efficient heat transfer between two fluids at different temperatures. The most common example of a heat exchanger is the automobile radiator (Figure 1-1) [2] in which heat from liquid coolant is absorbed and dissipated into the cold air blowing through the radiator. The coolant in turn removes heat from the engine and keeps its temperature under control.

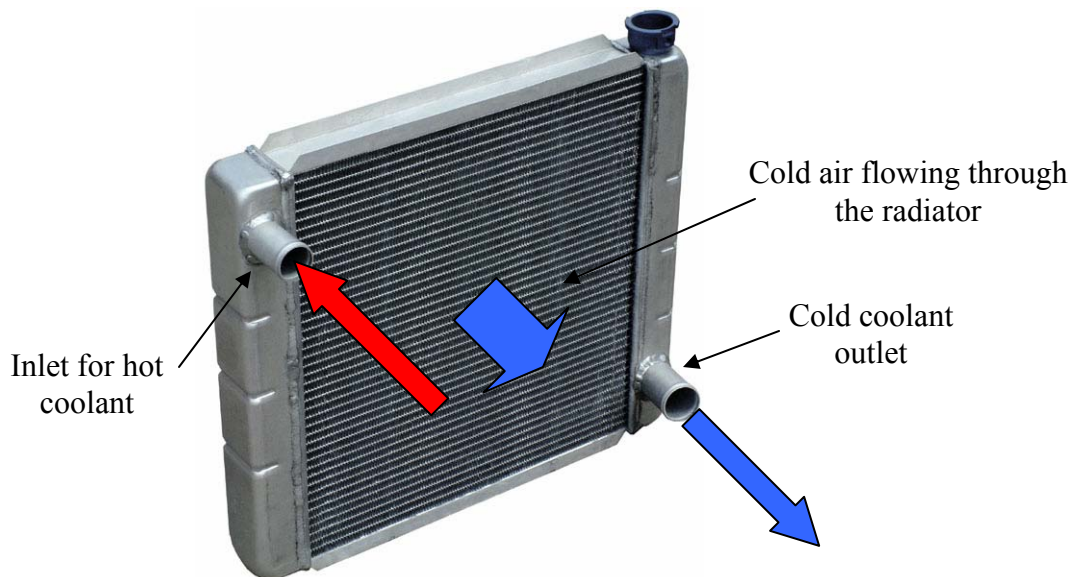


Figure 1-1. Common example of a heat exchanger: Automobile radiator. [Source: <http://www.answers.com/topic/radiator>]

Heat exchangers are ubiquitous in the refrigeration and air-conditioning industry, power plants, chemical plants, oil refineries and the manufacturing industry. They also find other applications such as waste heat recovery, space heating and electronic cooling. Several different heat exchangers of varied forms and structures are currently being used in the industry. The five main classification criteria for heat exchangers [3] and examples for each are listed in Table 1-1.

Of particular interest to us is the construction geometry known as extended surfaces, commonly referred to as heat fins. Heat fins are attachments or extrusions on a primary heat transfer surface that serve to increase the overall surface area, resulting in higher heat transfer.

Figure 1-2 is a picture of a finned surface [4] used to cool integrated circuit (IC) chips.

Table 1-1. Heat Exchanger Classification.

Classification criteria	Types
Basic operation	Recuperators and regenerators
Geometry of construction	Tubes, plates and extended surfaces
Flow arrangements	Parallel-flow, counter-flow and cross-flow
Transfer processes	Direct contact and indirect contact
Heat transfer mechanism	Single-phase and two-phase

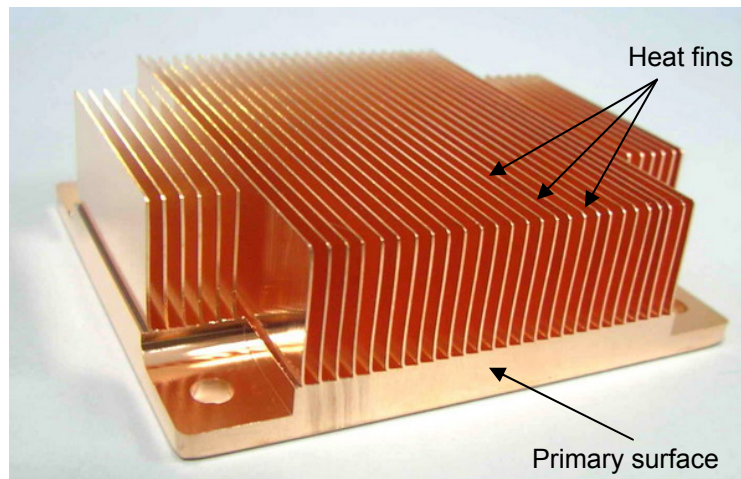


Figure 1-2. Extended surface heat exchanger used in electronic cooling. [Source: http://npowertek.trustpass.alibaba.com/product/11645462/NP_Skived_Fin_Heat_Sink.html]

Apart from their usage in gas-to-gas and gas-to-liquid heat exchangers, extended surfaces are also used to enhance heat transfer between a solid and a fluid – for instance in electric power transformers. In the strictest sense, such kind of device does not qualify as a heat exchanger as there is no fluid-to-fluid heat transfer. However, it is common practice in the literature [5], [6] to refer to these devices as heat exchangers anyways. The example in Figure 1-2, a heat sink, is one such device which enhances heat transfer from an IC (solid) to the ambient air (fluid).

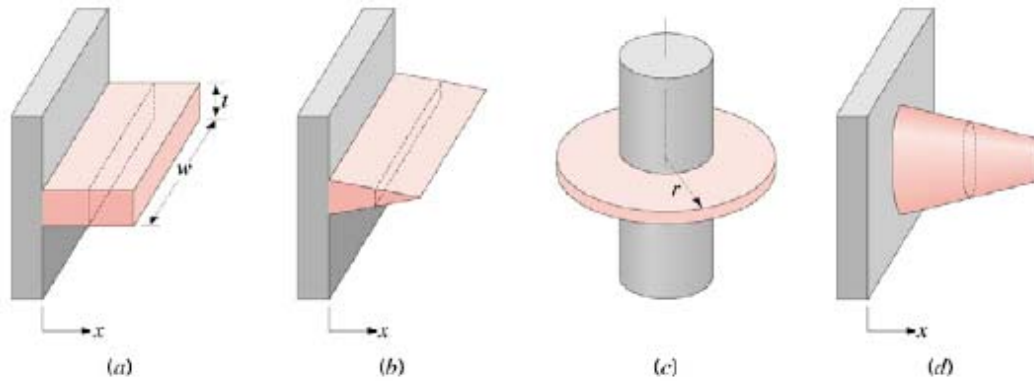


Figure 1-3. Different fin configurations. A) Rectangular fin. B) Triangular fin. C) Annular fin. D) Pin fin [Adapted from F. P. Incropera and D. P. DeWitt, *Fundamentals of Heat and Mass Transfer* (Page 128, Figure 3-14). John Wiley & Sons Inc., 2002]

Several different fin configurations are possible (Figure 1-3) [7], each catering to a different need. Typically, the fin material has high thermal conductivity and fins are commonly used in arrays rather than as single fins.

1.2 MEMS Heat Exchangers and Applications

A tremendous amount of research effort is devoted to the implementation of heat exchangers at the microscale for a wide range of applications. One of the oldest and widest application area for micro heat exchangers is microelectronic device cooling. As early as in 1981, Tuckerman and Pease [5] demonstrated the possibility of integrating a liquid-cooled micro heat exchanger (Figure 1-4) within the Si substrate, thereby eliminating the need for an external heat sink. Consequently, the concept of microchannel heat sinking was used for other similar applications such as cooling of laser diode arrays [8] and monochromator crystals [9]. Today, microelectronic cooling with integrated heat exchangers has evolved as a significant research topic in itself. The DARPA HERETIC (Heat Removal by Thermo-Integrated Circuits) program was commissioned to investigate this topic specifically.

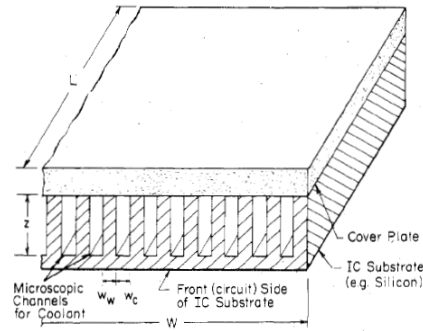


Figure 1-4. Compact heat sink implemented by Tuckerman and Pease. [Adapted from D. B. Tuckerman and R. F. W. Pease, “High-performance heat sinking for VLSI,” *IEEE Electron Device Lett.* (Figure 1), vol. EDL-2, no. 5, pp. 126-129, 1981]

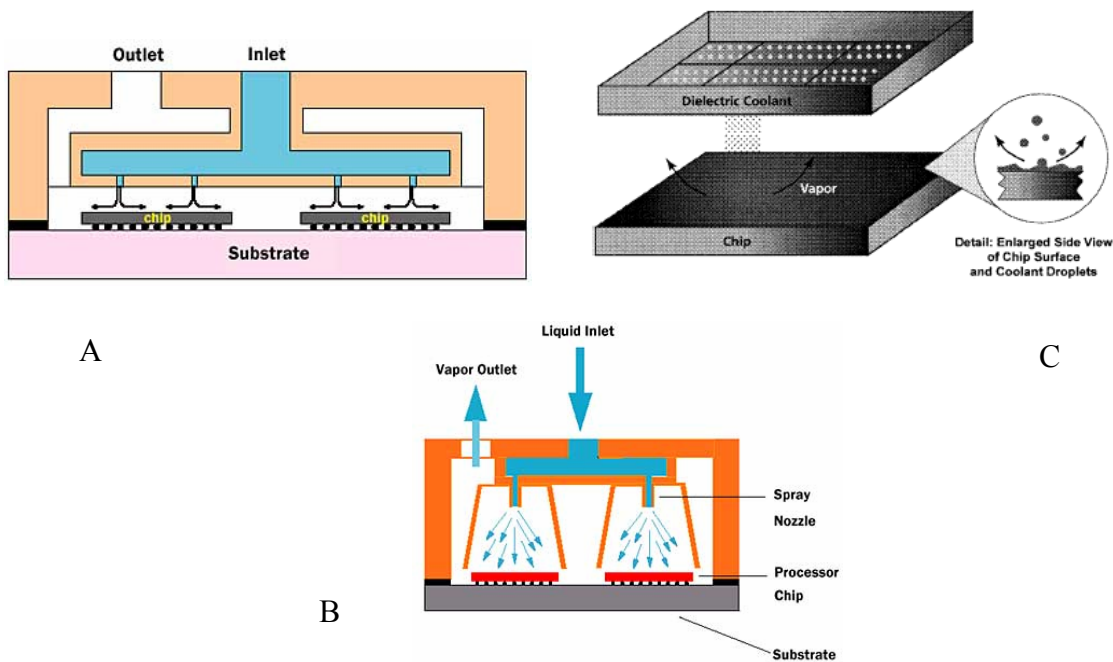


Figure 1-5. Improved MEMS electronic cooling methods. A) Jet impingement cooling. B) Spray cooling. [Reprinted with permission from Michael J. Ellsworth, Jr. and Robert E. Simons, “High Powered Chip Cooling - Air and Beyond,” *ElectronicsCooling*, (Figures 6 & 5), Volume 11, Number 3, pp. 14 – 22, August 2005] C) Droplet cooling [Adapted from C. H. Amon, J. Murthy, S. C. Yao, S. Narumanchi, C. F. Wu, and C. C. Hsieh, “MEMS-enabled thermal management of high-heat-flux devices EDIFICE: embedded droplet impingement for integrated cooling of electronics,” *Experimental Thermal and Fluid Science*, (Figure 2), vol. 25, pp. 231-242, 2001]

Many alternate and improved heat removal techniques have been and are being developed.

MEMS impinging jet cooling, illustrated by Wu [10] makes use of the fact that the heat transfer

coefficient of an impinging jet is an order of magnitude larger than conventional tangential fluid cooling. Research at Carnegie Mellon University focuses on the development of an embedded impingement cooling device using tiny droplets of dielectric coolants [11]. These micro-droplets are impinged from an array of micro-nozzles achieving a very high chip heat transfer rate. Another interesting technique is to spray the dielectric coolant liquid over the chip again using micro-nozzles [12] and allowing it to evaporate. Schematic views of the three heat removal techniques just described are shown in Figure 1-5.

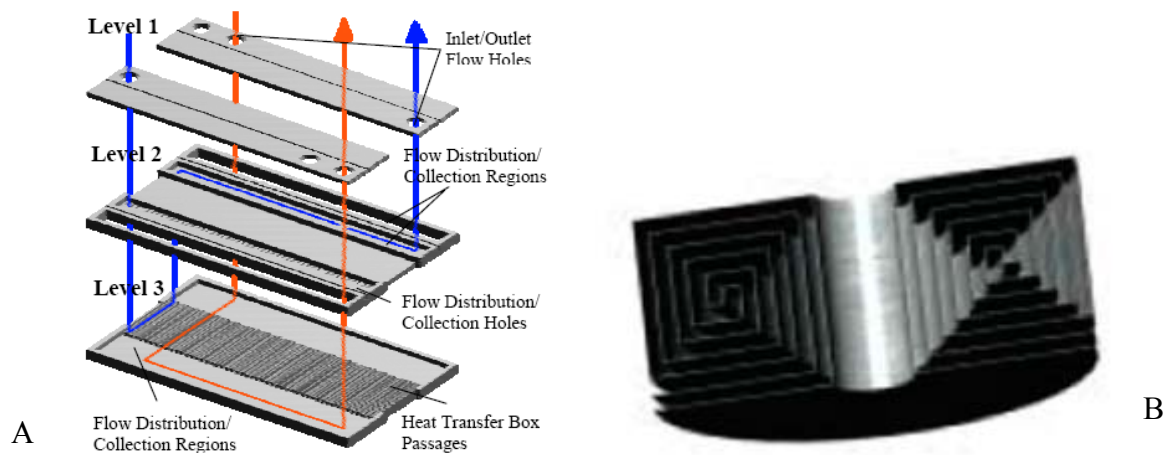


Figure 1-6. Micro heat exchangers for heat engines. A) Layered view of heat exchanger developed by Sullivan [S. Sullivan, X. Zhang, A. A. Ayon, J. G. Brisson, “Demonstration of a Microscale Heat Exchanger for a Silicon Micro Gas Turbine Engine,” *Transducers 01*, IEEE Piscataway, NJ, (Figure 2a) pp. 1606–1609, 2001], B) Swiss roll type combustor [L. Sitzki, K. Borer, E. Schuster, P.D. Ronney, and S. Wussow, “Combustion in microscale heat-recirculating burners,” in *Proc. of the Third Asia-Pacific Conference on Combustion*, Seoul, Korea, 24–27 June 2001, pp. 473–476]

An emerging application area where micro heat exchangers are increasingly used is micro heat engines. The purpose of heat exchangers in these devices is to absorb or deliver heat energy to a working fluid from external sources or to recuperate heat from exhaust gases. The microfabricated rankine cycle steam turbine demonstrated by Frechette [13] integrates two microchannel two-phase heat exchangers that function as an evaporator and condenser. As part

of the MIT's micro gas turbine project, a recuperative micro heat exchanger was developed and demonstrated by Sullivan (Figure 1-6(A)) [14]. In this design, heat is exchanged between the exhaust gases and the pre-combusted compressed air entering the engine in a radial counter-flow configuration. Using the same principle of recuperation, the Swiss-roll type combustor (Figure 1-6(B)) was built in USC [15]. The device has multiple windings of the reactant and the exhaust gas channel in a spiral configuration resulting in a very high heat transfer surface area [16]. Both 2D and 3D type exchangers were demonstrated.

Yet another important and promising use of microscale heat exchangers is thermoelectric (TE) cooling and power generation. As TE power generation forms the focus of the thesis, various existing implementations of micro heat exchangers for TE generation are reviewed in a later section.

1.3 Thermoelectric Power Generation

Thermoelectric power generation is the process of direct conversion of thermal energy in the form of a temperature gradient into electricity. It works based on the principle of thermoelectric effect which can be described as follows: the junction between two dissimilar metals generates a voltage when the junction temperature is higher than the ambient temperature. The principle is illustrated in Figure 1-7. Similarly when an electric current is passed through the junction of dissimilar materials, it results in a temperature change at the junction. Although the above is a simplified statement of the thermoelectric effect, the term 'thermoelectric effect' is actually a single term that represents the combination of three separately identified physical effects namely the Seebeck effect, Peltier effect and the Thomson effect. These three effects [17] are described below:

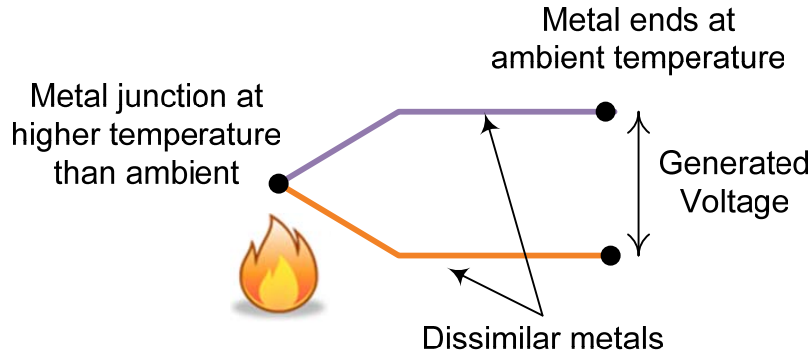


Figure 1-7. Thermoelectric effect

1.3.1 Seebeck Effect

When junctions of two dissimilar conductors are maintained at different temperatures, a voltage is developed between them. The developed voltage is a function of the difference in temperature and the material properties of the conductors.

$$V = \alpha \Delta T \quad (1-1)$$

where, V is the voltage developed because of Seebeck effect (V), α is the Seebeck coefficient (V/K), a constant dependent on material properties, and ΔT is difference in temperature between the junctions (K).

1.3.2 Peltier Effect

When electric current flows between two dissimilar conductors held at a constant temperature, heat is either absorbed or released at the junction depending on the direction of the current flow. The amount of heat is again dependent on the materials and the magnitude of current flowing through the junction.

$$Q = \pi I \quad (1-2)$$

where, Q is heat flow at the junction due to Peltier effect (W), π is the Peltier coefficient (W/A), a constant dependent on material properties, and I is the current flowing through the junction (A).

1.3.3 Thomson Effect

When electric current flows through a single material under a given temperature gradient, heat is either absorbed or released by the material depending on the direction of current flow.

The amount of heat is proportional to the magnitude of current, the material and the temperature gradient across the material.

$$\frac{dQ}{dx} = \tau I \frac{dT}{dx} \quad (1-3)$$

where, $\frac{dQ}{dx}$ is the heat flow per unit length due to Thomson effect (W/m), τ denotes Thomson coefficient (V/K), a constant dependent on material properties, I is the current flowing through the material (A), and $\frac{dT}{dx}$ represents the rate of change of temperature with respect to length of the material (K/m).

1.3.4 Thermoelectric Generator

A thermoelectric generator (TEG) is a device which converts thermal energy into electrical energy based on the principle of the thermoelectric effect. In its simplest form, it has three main elements, namely the heat source, the heat sink and the thermopile. The heat source is at a higher temperature than the heat sink, and the temperature difference between them creates the required temperature gradient across the thermopile. The thermopile is made up of large number of alternating thermoelectric materials connected electrically in series and thermally in parallel; each pair of different TE materials is called a thermocouple. In the presence of a temperature gradient, an electric potential is generated between the ends of the thermopile and current flows through any electrical load that is connected in series with the thermopile.

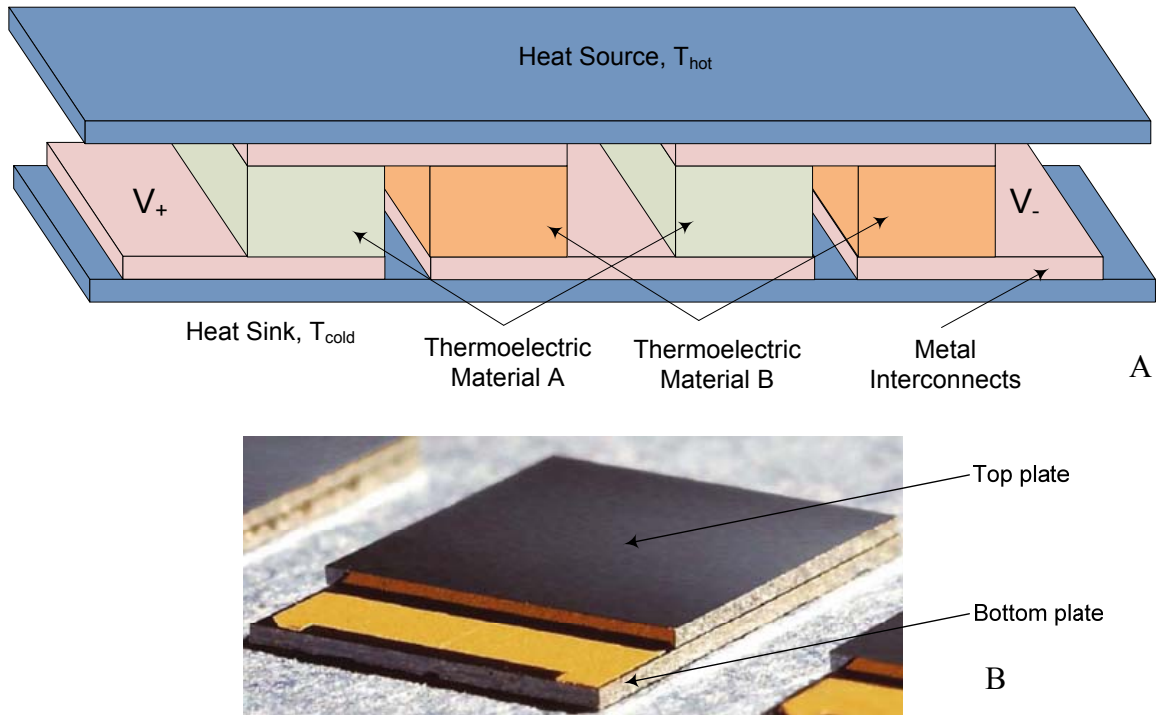


Figure 1-8. Basic thermoelectric generator. A) Schematic view. B) Photograph [Adapted from Thin Film Peltier Cooler, MPC-D901 Datasheet, www.micropelt.com]

Figure 1-8 shows the schematic of a standard parallel plate TE device and a commercial TE device [18]. The heat source and heat sink plates are generally highly thermally conductive, and thus are usually assumed to each be at a uniform temperature. In real world implementations of TEG, the source of heat could be radioactive decay, hydrocarbon fuel combustion or even automobile exhaust. The heat sink is typically interfaced to ambient air, but in special cases, it could be a coolant such as water or helium. For the particular configuration shown, voltage is generated with polarities as indicated; however, in reality the voltage polarity is dependent on the material properties of the constituent thermoelectric materials. For this simple TEG, the generated open circuit voltage, V_{oc} is given by

$$V_{oc} = n\alpha\Delta T, \quad (1-4)$$

where, n is the number of thermocouples, α is the Seebeck coefficient, constant for a given pair of TE materials, and ΔT is the difference between T_{hot} and T_{cold} .

As is obvious, for a given material and number of thermocouples, the generated voltage, V_{oc} is directly proportional to the temperature difference, ΔT between the heat source and heat sink. In order to efficiently transfer the heat energy from the source to the hot side of the thermopile and to reject heat from the cold side of the thermopile to the sink, heat exchangers can be attached to the hot and cold plates. These heat exchangers thus serve to enhance ΔT and thereby improve overall TEG efficiency. Figure 1-9 shows a TEG with integrated extended surface heat exchangers.

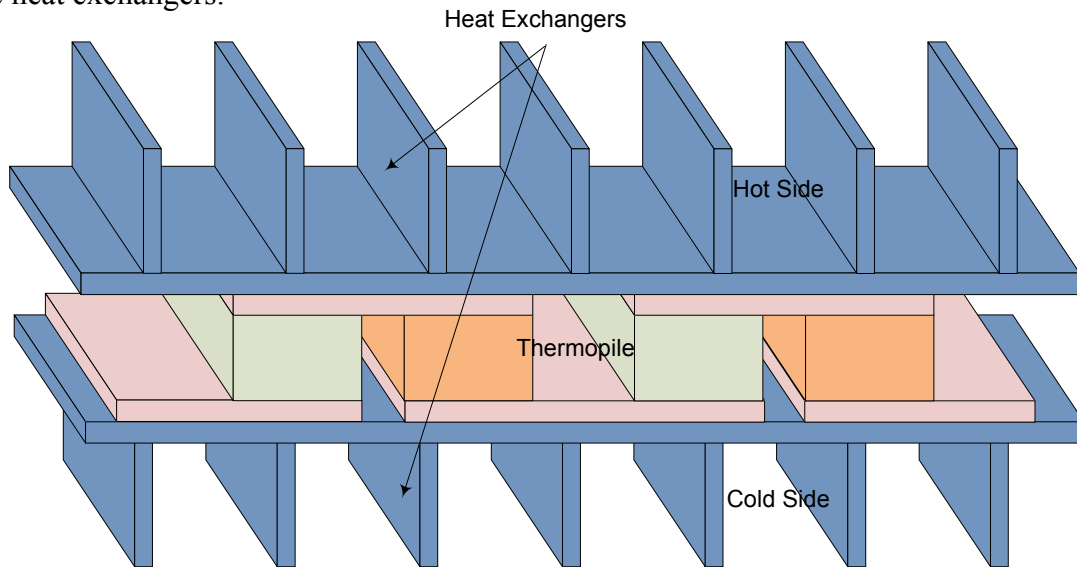


Figure 1-9. TE generator with integrated heat exchangers

1.4 Microscale TE Generators

With the recent developments in MEMS technology and the advent of high performance thin film TE materials [1], microscale TE generators are becoming increasingly popular especially due to the growing need for portable power sources. TE generation stands to benefit at a microscale especially because of the increase in the surface area-to-volume ratio [19] – a

greater surface area means higher exposure to the heat source and sink resulting in a higher ΔT . This advantage is countered, however, by the increasing thermal leakage between the hot and cold sides of the thermopile as they get closer and closer in a microscale device. Again, by integrating heat exchangers with the TEG device, some efficiency improvement can be achieved.

There have been several implementations of microscale TE generators aimed at generating electrical energy from a wide variety of heat sources. One example is the combustion-based TE power generator [20] demonstrated by Schaevitz at MIT (Figure 1-10(A)). The device used silicon-germanium thermopiles on bulk micromachined Si substrate to generate power while the source of heat was catalytic combustion of hydrocarbon fuels such as hydrogen, ammonia, and butane. Reportedly, the efficiency of the device was very low because of thermal leakage - 0.01% for a ΔT of 400 °C. The poly-Si based micro TEG developed by Strasser [21] at Infineon, on the other hand, used simple BiCMOS surface micromachining techniques to fabricate the device. The device (Figure 1-10(B)) achieves an open circuit voltage of less than 200 mV/K, limited by the electrical resistance of the thermocouple legs. The Swiss-roll combustor based thermoelectric power generation system, microFIRE [16] developed by Cohen and others at USC is yet another TEG that uses combustion as its energy source. The salient feature of this implementation is that both the thermoelectric generator and the heat exchanger are integrated in a single system thereby enhancing the overall system efficiency.

As can be seen from the examples cited, TE generators generally suffer from low conversion efficiencies at microscale due to issues such as thermal leakage and high electrical resistance. Although not always feasible, integration of heat exchangers within the TE device can result in a higher temperature gradient and hence an improved system efficiency.

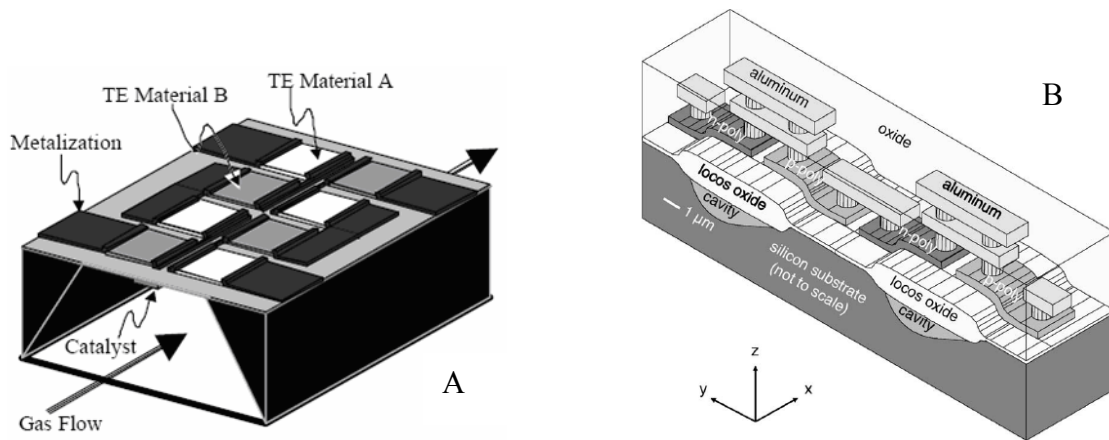


Figure 1-10. Examples of micro TEGs. A) Combustion based TEG developed by Schaevitz [S. B. Schaevitz, A. J. Franz, K. F. Jensen, and M. A. Schmidt, “A combustion-based MEMS thermoelectric power generator,” in *Proc.—11th Int. Conf. on Solid-State Sens. and Act. (Transducers '01)*, (Figure 1b), 2001], and B) polysilicon – poly SiGe TEG developed by Strasser [M. Strasser, R. Aigner, M. Franosch, G. Wachutka, “Miniaturized thermoelectric generators based on poly-Si and poly-SiGe surface micromachining,” in *Proc.—11th Int. Conf. on Solid-State Sens. and Act. (Transducers '01)*, (Figure 6, Page 539), 2001]

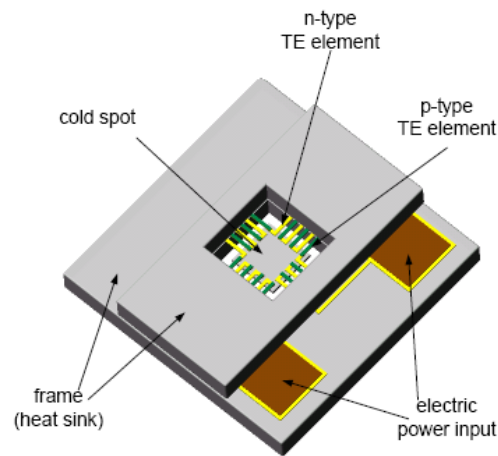


Figure 1-11. Concept of thermoelectric cooling. [D.-Y. Yao, C.-J. Kim, and G. Chen, “Design of Thin-Film Thermoelectric Microcoolers,” in *ASME International Mechanical Engineering Congress & Exposition*, (Figure 1, Page 2), Orlando, Florida, November 5-10, 2000]

Microscale thermoelectric coolers (TECs) also find extensive applications including cooling of microelectronics, charge coupled devices (CCDs) and other MEMS devices such as resonators and infra-red sensors [22]–[24]. TECs are devices that operate in Peltier mode, in

contrast to TEGs which operate in Seebeck mode. However, the design considerations and challenges for TECs and TEGs are similar; especially, thermal isolation between the ends of thermocouples is a must in both devices. Figure 1-11 illustrates the concept of thermoelectric cooling.

1.5 Research Goals

The goal of this research work is to design, fabricate and test a microscale heat exchanger platform that can extract waste heat energy from the exhaust of small combustion engines and maintain a temperature gradient across a thermopile. The thermopile, in turn, converts the temperature gradient into electric potential. This work is part of a larger research effort to develop a thermoelectric microgenerator that could serve as a small and efficient portable soldier power system. Therefore, the heat exchanger design needs to meet the constraints placed by the thermopile design.

By design, the thermopile is made of thin film materials that require a suitable substrate such as silicon for deposition and processing. This implies that the heat exchanger platform also should be made out of silicon for ease of fabrication. Another important criterion is to minimize the leakage between the hot and cold side of the thermopile while still keeping the device structurally stable. In addition to these, the heat exchanger should improve system performance by coupling the maximum possible heat energy from the exhaust to the thermopile.

1.6 Thesis Outline

The thesis is organized in five chapters. This chapter has provided the necessary background on heat exchangers and thermoelectric power generation. It reviewed a few of the several existing implementations of microscale heat exchangers, TE generators, and their attributes, and also identified the goals of the research, the constraints and challenges involved.

Chapter 2 elaborates on the various different device design requirements and describes how a particular device structure is chosen amongst others. It also explains the how the device dimensions are arrived at based on a first-order thermal circuit model; later, a detailed thermal model of the device to be built is also developed. This is followed by a discussion of the theoretical model based performance predictions.

Chapter 3 gives a detailed description about the fabrication of the heat exchanger device. It explains the choice of different materials and methods and also discusses about the bonding and stacking procedures.

Chapter 4 details the experimental setup and procedure and presents the results obtained through laboratory testing of the device for different temperature and flow conditions. The results are compared with the predictions of the theoretical MATLAB model.

Chapter 5 summarizes the major results, draws conclusions and gives suggestions for improvements and future work.

CHAPTER 2 HEAT EXCHANGER DEVICE DESIGN AND MODELING

This chapter focuses on the design and modeling of the heat exchanger platform onto which the thermopile is to be incorporated. As described earlier, the heat exchanger is designed to both absorb heat energy from engine exhausts and create a temperature gradient across a thermopile. The thermopile consists of multiple legs of dissimilar materials connected thermally in parallel but electrically in series. By virtue of the thermoelectric properties of the materials, this thermopile produces electric power from the temperature gradient established by the heat exchanger. In a thermoelectric generator (TEG), the thermopile and the heat exchanger are integrated into the same device, thus forming a complete system that converts waste heat into useful power. The heat exchanger design for such a system should therefore be optimized for the best performance of the overall system, i.e. to generate maximum power rather than to create maximum temperature gradient.

Also, because of the small physical dimensions at the microscale, thermal leakage from the hot region to the cold region of the heat exchanger becomes significant and presents a serious design issue. A high thermal leakage (resulting in low temperature differentials) causes the heat exchanger efficiency to fall to extremely low values. The problem of high thermal leakage in microscale TEGs and the resultant low thermal efficiency is widely acknowledged in literature [20], [21]. To avoid this leakage, it becomes necessary to thermally isolate the hot and cold regions of the heat exchanger. However, by definition, the TEG has multiple thermocouple legs extending from the hot region to the cold region, thereby offering a direct thermal path between them. The thermocouple legs are obviously necessary, and materials that offer high thermoelectric function with low thermal conductivity are the focus for material optimization. From the heat exchanger design standpoint, the goal then is to eliminate or minimize all thermal

paths other than the thermoelements themselves. Once this is achieved, the overall thermoelectric generator can be designed to generate reasonable amount of electric power. The design of the structure and layout of the thermopile is beyond the scope of this thesis. However, since the design of heat exchanger and thermopile are strongly interrelated, assumptions and details on thermopile design will be described wherever necessary.

2.1 Thermopile Material and Arrangement

For the design of this heat exchanger, the following assumptions are made with regard to the thermopile: First, the thermocouples are made of two different thin-film thermoelectric materials such as p- and n-type thin film IV-VI semiconductor or alternatively two dissimilar metals. Typical examples of IV-VI semiconductors that have good thermoelectric properties are alloys such as Bi_2Te_3 , BiSbTe , PbTe , and PbSeTe . It should also be mentioned here that these doped semiconductors offer better thermoelectric performance compared to typical metals. Second, it is assumed the thermopile requires a silicon substrate for deposition and processing [25]. A thin layer of thermally grown SiO_2 electrically insulates the thermopiles from the conductive Si substrate; the oxide layer also serves as the buffer layer required for vapor deposition of IV-VI semiconductor [26].

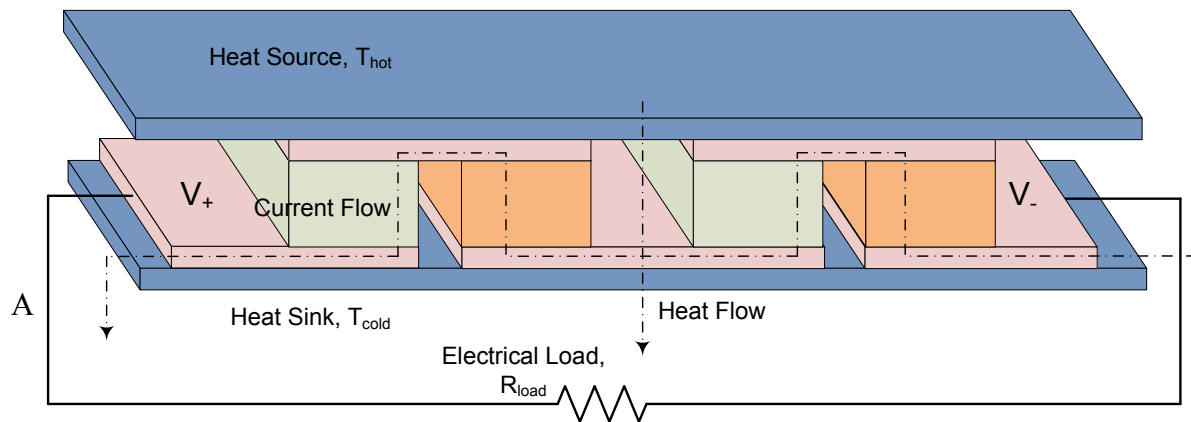


Figure 2-1. Thin-film TEG. A) Out-of-plane configuration B) In-plane configuration

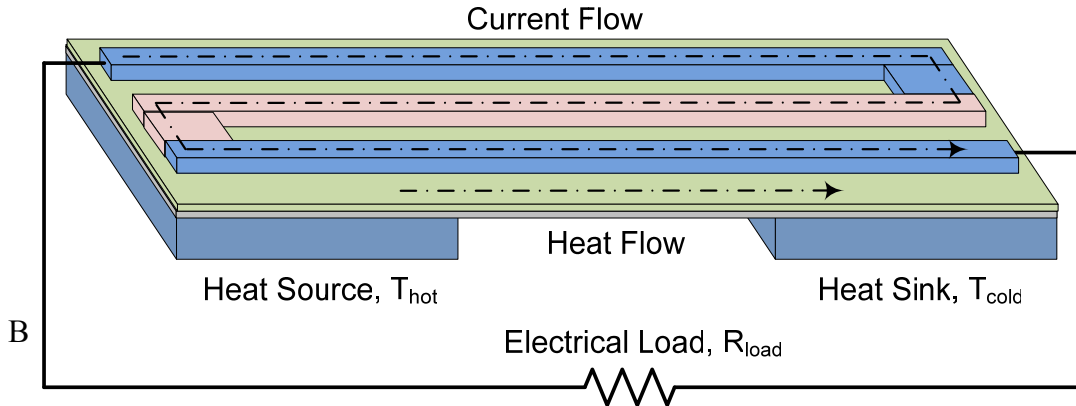


Figure 2-1. Continued.

The thermocouples can either be arranged in an in-plane fashion where current and heat flow parallel to the substrate or out-of-plane where current and heat flow perpendicular to the substrate. Typical implementations of the in-plane and out-of-plane configurations are shown in Figure 2-1.

2.2 Structure of Thermoelectric Microgenerator

A variety of requirements need to be satisfied while deciding the structure of the TEG. Some of the important requirements can be explained by referring to the simple in-plane TE generator (Figure 2-2(A)). The TEG is assumed to consist of multiple thermocouple legs on top of a silicon substrate; temperature gradient is created by the flow of hot and cold fluids through channels at both ends of the device. A thermally conductive but electrically insulating supporting membrane separates the thermocouples from the substrate; there is also a thin sheet of silicon underneath the membrane to provide additional support to the thermocouples.

The first-order model (Figure 2-2(B)) consists of an electrical and a thermal equivalent circuit. However, since the focus of this work is on the thermal performance of the device, the electrical part of the model will be discounted for the rest of the thesis. This simplified model assumes 1-D heat transfer from hot to cold side and ignores convection and radiation from the device surfaces. Each element in the model corresponds to a lumped thermal resistance in the

device: θ_{convh} and θ_{convc} represent the thermal resistance due to convective heat transfer from the hot and cold fluids, respectively, to the silicon substrate, θ_{TEG} is the effective conductive thermal resistance of the thermocouple legs, $\theta_{leakage}$ corresponds to the conductive thermal leakage of the supporting structures between the hot and cold sides, and θ_{Si} models the conductive thermal resistance from the fluid channels to thermocouple ends on both sides. T_{hfluid} and T_{cfluid} represent hot and cold fluid temperatures respectively.

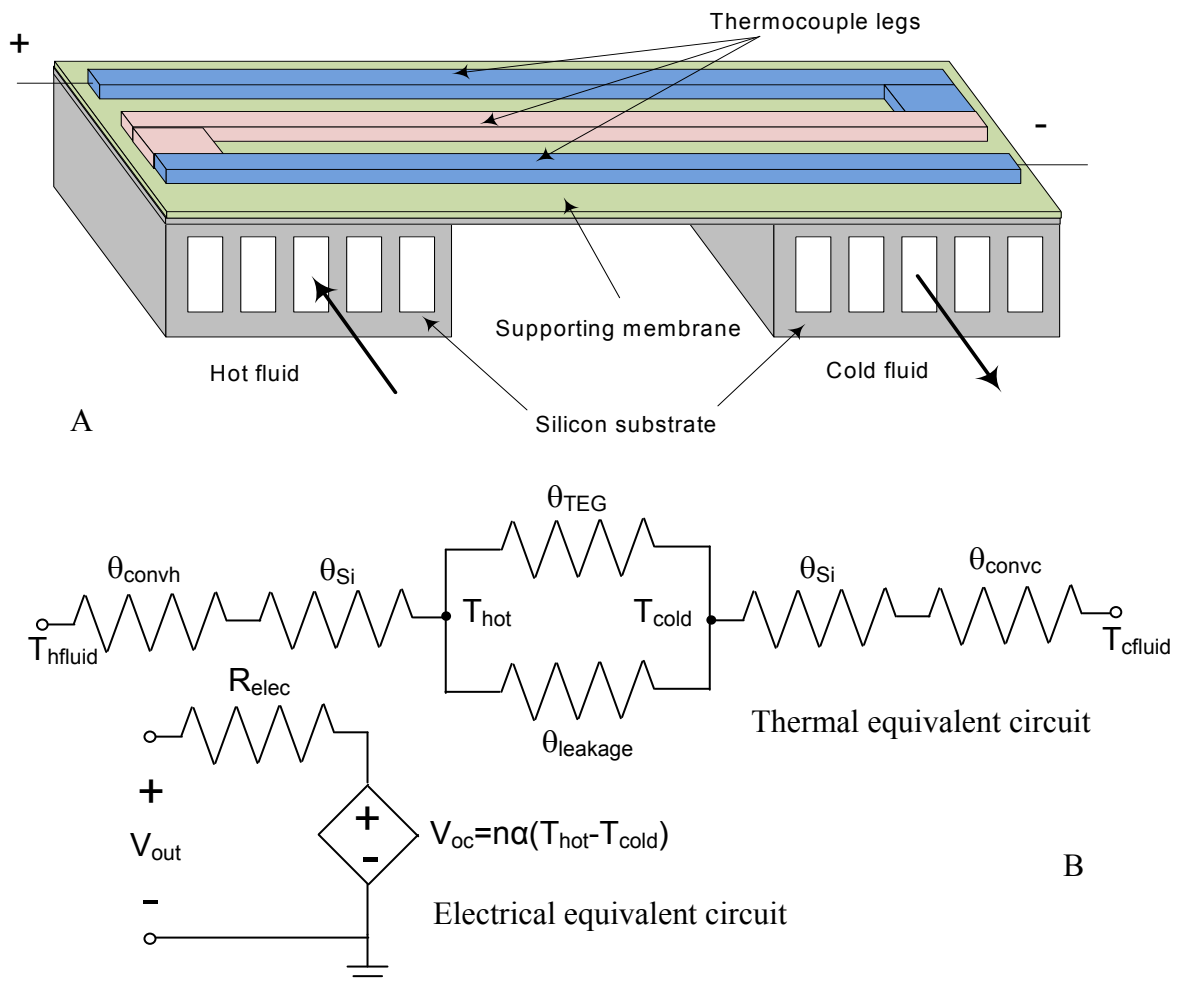


Figure 2-2. Planar TEG structure. A) Schematic view. B) Equivalent model.

For the simple TEG shown above, the expression for the maximum generated output power P_{out} is given by

$$P_{out} = \frac{V_{oc}^2}{4R_{elec}}, \quad (2-1)$$

where, V_{oc} is the generated open circuit voltage and R_{elec} is the electrical resistance of the thermopile. The open circuit voltage is in turn given by Equation 1-4 and is repeated here for convenience

$$V_{oc} = n\alpha\Delta T; \quad (2-2)$$

where, n represents the number of thermocouple legs, α is the Seebeck coefficient and ΔT is the difference between T_{hot} and T_{cold} . It can be seen from Equations 2-1 and 2-2 that the output power of the TEG has a quadratic dependence on the temperature gradient across the thermopile. Thus, ΔT is an important factor that affects the device power output.

Based on the thermal equivalent circuit shown in Figure 2-2(B), ΔT can be expressed in terms of the various device thermal resistance components. In the equations that follow, and in rest of the thesis, the symbol “||” denotes a parallel combination of resistances. For example, the parallel combination of thermal resistances θ_A and θ_B is given by the expression

$$\theta_A \parallel \theta_B = \frac{\theta_A \theta_B}{\theta_A + \theta_B}$$

$$\Delta T = \frac{(\theta_{TEG} \parallel \theta_{leakage})(T_{hfluid} - T_{cfluid})}{\theta_{convh} + \theta_{convc} + 2\theta_{Si} + (\theta_{TEG} \parallel \theta_{leakage})} \quad (2-3)$$

Equation 2-3 shows ΔT increases with the temperature difference between the heat source, T_{hfluid} and heat sink, T_{cfluid} , which is rather intuitive. It also shows that ΔT is inversely proportional to the convective thermal resistances, θ_{convh} and θ_{convc} , and θ_{Si} , indicating that these resistances should be minimized. It can also be inferred that ΔT increases as $\theta_{TEG} \parallel \theta_{leakage}$ increases relative to the sum of thermal resistances, θ_{convh} , θ_{convc} and θ_{Si} , indicating that θ_{TEG} and

$\theta_{leakage}$ should be maximized. The thermocouple resistance, θ_{TEG} is a function of the dimensions and number of the thermocouple legs, and is fixed for a given thermopile design. It is important to mention here that if θ_{TEG} is increased with the aim of achieving higher ΔT , there is also an indirect increase in the electrical resistance R_{elec} which results in decreased P_{out} . This implies that a maximum ΔT across the thermopile need not necessarily imply maximum P_{out} . A better way to improve ΔT and achieve high output power is to minimize $\theta_{leakage}$ or the convective thermal resistances θ_{convh} and θ_{convc} as these do not affect R_{elec} . $\theta_{leakage}$ is the thermal resistance contributed by the thermal leakage paths through the thin silicon underneath the thermopile and the supporting membrane. Leakage due to conduction and convection of air between the hot and cold sides is ignored in this model.

The first requirement of a TEG structure is that the thermal leakage between the hot and cold sides of the TEG be minimal. It should be noted that a low thermal leakage implies high leakage thermal resistance, $\theta_{leakage}$; an ideal device with zero thermal leakage would therefore have infinite $\theta_{leakage}$. With an increase in $\theta_{leakage}$, the term $\theta_{TEG} \parallel \theta_{leakage}$ approaches its maximum value of θ_{TEG} , resulting in enhanced ΔT .

Expressions for both θ_{TEG} and $\theta_{leakage}$ can be obtained from Fourier's law for 1-D longitudinal heat conduction [7]. For a general case, the conductive thermal resistance, θ of a material is given by

$$\theta = \frac{l}{kA} \quad (2-4)$$

where l is the length of the material, k is its thermal conductivity, and A is the area of cross-section. Based on Equation 2-4, θ_{TEG} can be written as

$$\theta_{TEG} = \frac{1}{n} \left(\frac{l_{TEG}}{k_{TEG} A_{TEG}} \right), \quad (2-5)$$

where, l_{TEG} , k_{TEG} , and A_{TEG} represent corresponding quantities for the individual thermoelements. Division by n , the number of thermocouple legs is to account for the n parallel thermal paths between the hot and cold regions. Similarly, $\theta_{leakage}$ is given by

$$\theta_{leakage} = \left(\frac{l_{mem}}{k_{mem} A_{mem}} \right) \parallel \left(\frac{l_{Si}}{k_{Si} A_{Si}} \right), \quad (2-6)$$

where, l_{mem} , k_{mem} , and A_{mem} are the length, thermal conductivity, and cross-sectional area of the supporting membrane, while, l_{Si} , k_{Si} , and A_{Si} denote similar quantities for the thin sheet of silicon underneath the membrane.

The second requirement of a TEG structure is good fluid-solid convective heat transfer at the two ends of the thermopile. When stated in terms of the thermal resistances, the requirement is to minimize the convective thermal resistances θ_{convh} and θ_{convc} , and θ_{Si} . From heat transfer theory [7], the convective thermal resistance is given by

$$\theta_{conv} = \frac{1}{hA_s}, \quad (2-7)$$

where h is the convection heat transfer coefficient and A_s is the surface area where convection heat transfer takes place. For the TEG in Figure 2-2(A), the convection surface area is the sum of inner peripheral surface areas of the fluid channels. A common method employed to meet this requirement is to increase the convective surface area A_s by using heat fins. For the planar TEG, this can be achieved by creating multiple fluidic channels as shown and/or introducing internal fins in the fluid channels. Alternatively, h can also be increased; h is generally dependent on fluid properties such as velocity, viscosity and thermal conductivity, and the nature of fluid flow

such as natural convection or forced convection. In natural convection, the fluid motion occurs without any external source and offers only a low h values. In contrast, a forced convection can achieve very high h , but requires an external source such as a pump or fan, thereby reducing the net power efficiency of the TEG.

Some of the other critical requirements include the structural stability of the device and ease of fabrication and integration of the heat exchanger with the thermopile. Another practical requirement arises from device's intended application – energy harvesting. The fluid channel that extracts the heat energy from the exhaust gas also creates a fluidic backpressure on the exhaust outlet of the small combustion engine. Beyond a certain limit, this backpressure would affect normal operation of the engine. Therefore, the fluidic resistance offered by the hot gas channels should be sufficiently low. Finally, while meeting all these requirements, the dimensions of the device should still be in the microscale.

A few different TEG device structures were evaluated based on these requirements. Following is a brief description of each of the structures, an outline of their fabrication strategy, and their pros and cons as TE generators.

2.2.1 Simple in-Plane TEG Structure

The simplest form of TE generator is the in-plane structure (Figure 2-2(A)). Fabrication of the thermopile in this TEG is straightforward, and involves patterning and deposition of the chosen thermoelectric materials on the Si substrate. On the other hand, formation of the closed fluid channels on either side of the device is involved and requires selective etching and bonding of multiple micromachined substrates to form the closed channels.

The major disadvantage of this TEG structure, however, is the existence of the thin sheet of silicon underneath the thermocouples. It offers a large thermal path for the heat flux from the hot side to cold side of the device resulting in huge thermal leakage. This silicon is essential for

the mechanical stability of the entire structure and hence cannot be removed; without it, the rectangular structure would simply break. Some of the other concerns include large fluidic resistance of the channels – the channel height is limited by the thickness of Si wafer which is usually only 500-600 μm , and difficulty in coupling the exhaust gas from the engine to the TEG. Top and cross sectional views of the device are shown in Figure 2-3.

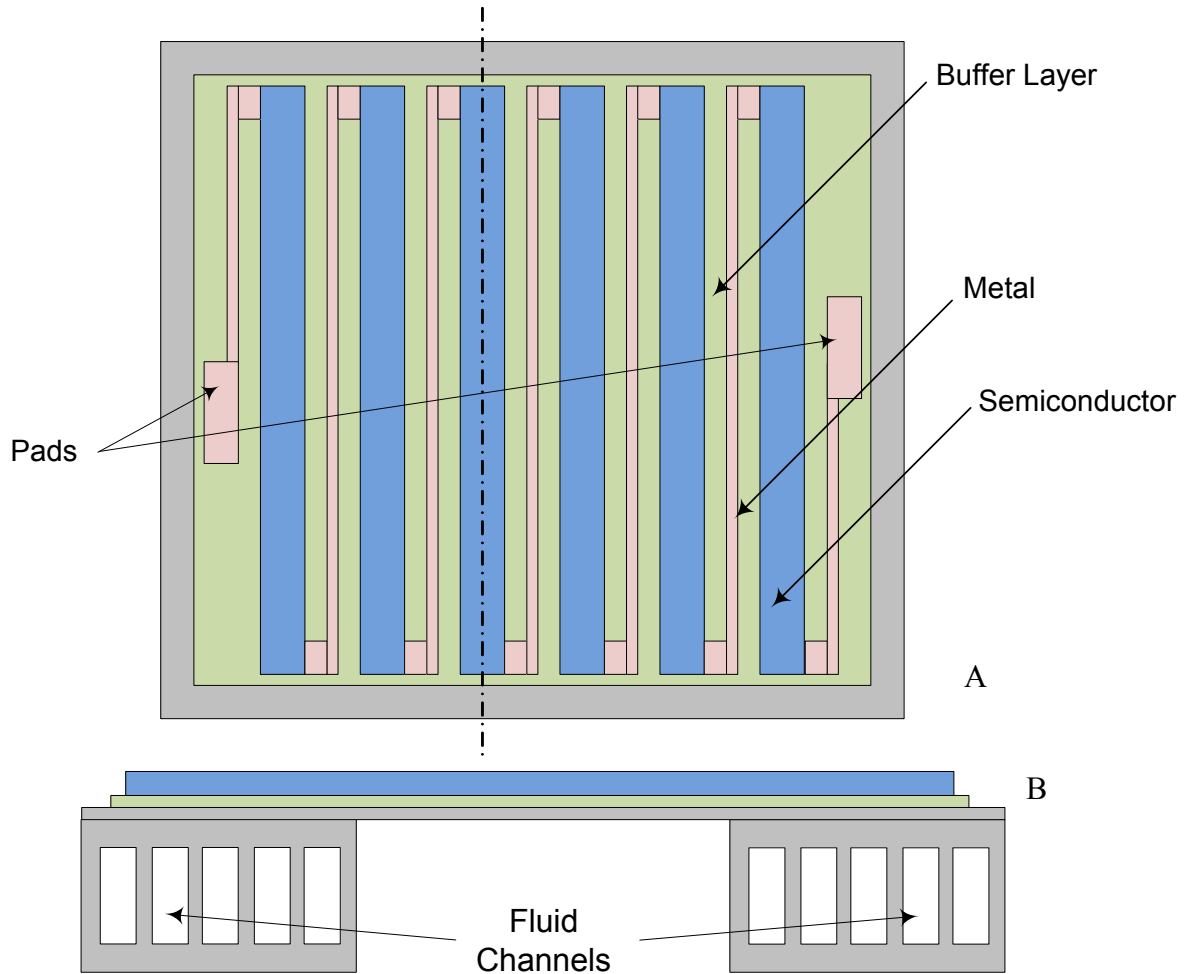


Figure 2-3. In-plane TEG. A) Top view. B) Cross sectional view.

2.2.2 Out-of-Plane Flip-Chip Bonded Structure

The next structure that was evaluated is an out-of-plane structure, as employed almost exclusively in macroscale devices. The schematic view of the out-of-plane TEG is shown in Figure 2-4. The thermopile is made up of alternating p- and n-type thermoelectric pillars

connected by metal interconnects and arranged in meanders for area efficiency. In contrast to the in-plane structure, the device here is vertically configured with both heat and current flowing perpendicular to the surface of the semiconductor thin film. The entire structure is sandwiched between two silicon plates and is suitably insulated by buffer layers. A temperature gradient is created by the hot exhaust gas flowing through channels in top plate while the bottom plate is at room temperature; alternatively the bottom plate can also have channels or fins to improve the temperature gradient.

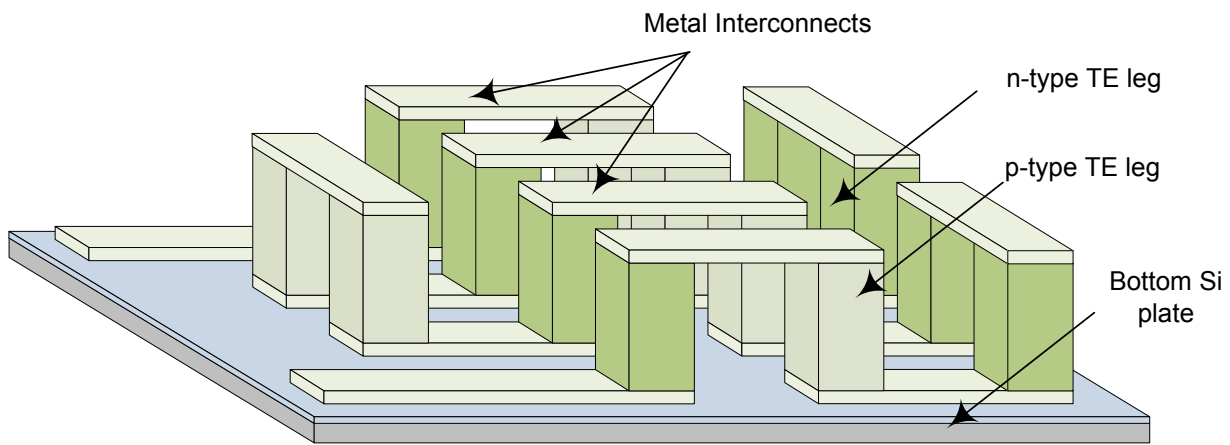


Figure 2-4. Out-of-plane TEG with top Si plate removed.

One key advantage of the out-of-plane structure is that the hot and cold silicon plates are connected only by the thermocouple legs and hence can result in low thermal leakage. However, it should be noted that the plates themselves are separated only by the height of thin semiconductor film (10 to 50 μm), and radiative or convective heat transfer could supersede the conductive pathway. From a fabrication perspective, the complexity involved is much greater than the in-plane design. The p- and n-type TE legs have to be deposited on different substrates and then flip-chip bonded. The integration of the fluid channels necessitates a selective etch and another step of wafer bonding. Concerns related to fluidic coupling and channel fluidic resistance apply to this structure as well.

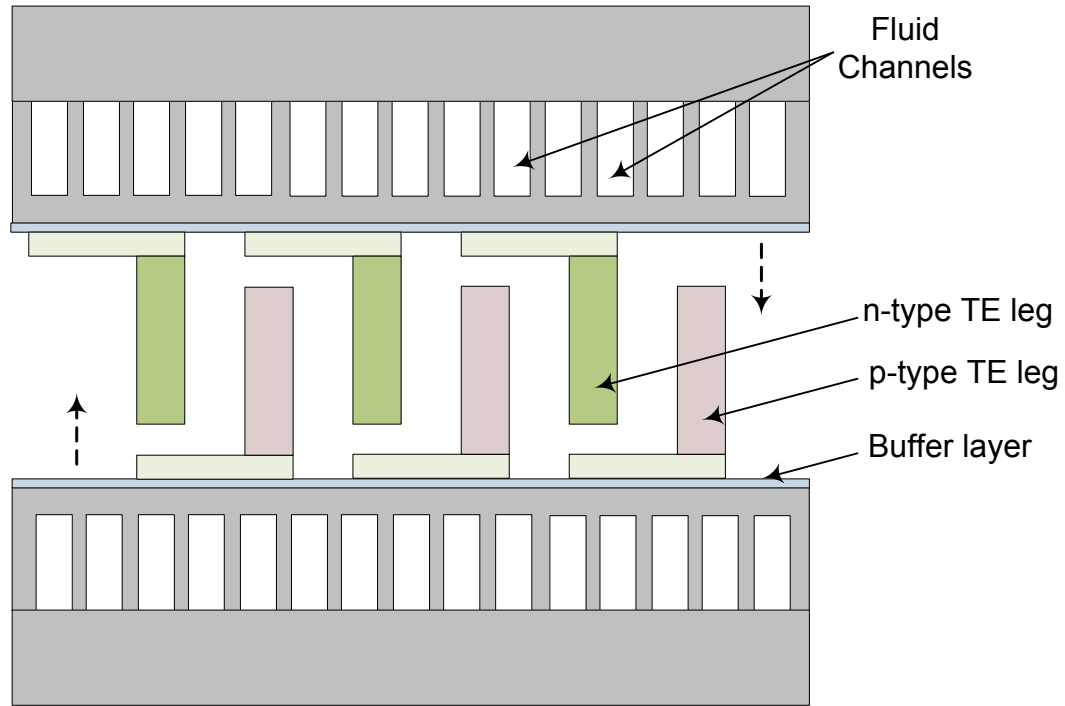


Figure 2-5. Thermopile formation in out-of-plane TEG.

2.2.3 Vertically Stacked Thermopile Structure

A stacked thermopile structure (Figure 2-6) takes advantage of the planar processing techniques to build several alternate layers of n- and p-type thin film TE material sandwiched between buffer layers on top of a silicon substrate. Metal interconnects serve to complete the electrical connectivity. When integrated with a suitable heat exchanger that creates a lengthwise temperature gradient, the structure would have the highest power density among the various structures discussed.

The greatest disadvantage of this structure is the difficulty in integrating a suitable heat exchanger, which also makes it inappropriate for the application in hand. Thermal leakage from the hot region to the cold region is mostly limited to the thermocouples, under the assumption that the silicon substrate is etched away. However, complete removal of silicon renders the

device fragile, implying a trade-off between thermal leakage and mechanical robustness.

Another concern is the excessive process time required to deposit multiple layers of TE material.

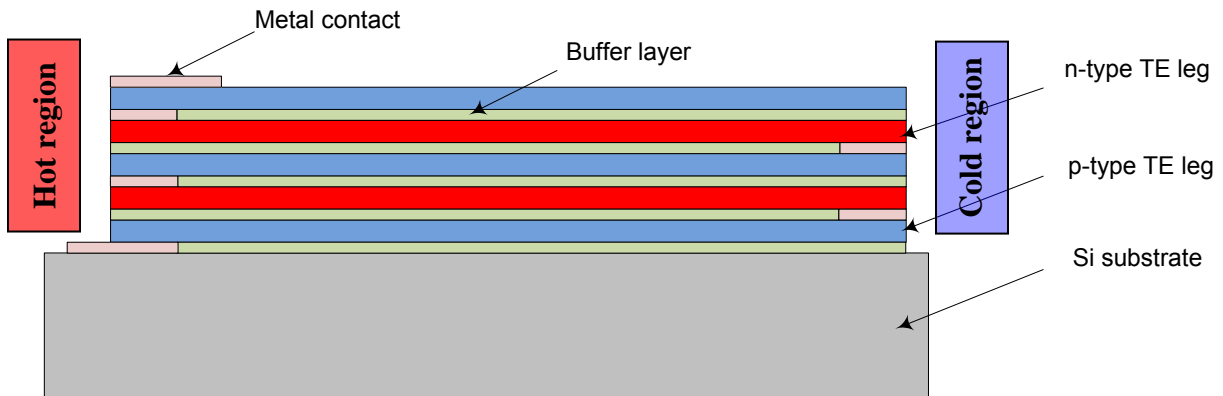


Figure 2-6. Vertically stacked thermopile structure.

2.2.4 Vertically Stacked Radial In-plane Structure

The stacked radial in-plane device exploits the concept of stacking to form two coaxial silicon pipes connected by several layers of radially oriented thermocouples. The inner pipe serves as a passage for the hot exhaust gas, while the outer pipe is at ambient temperature. By virtue of this arrangement, a radially-directed temperature gradient is created across the thermocouples.

To realize the tubular structure described above, multiple thermoelectric (TE) modules are fabricated and stacked one above the other. Each TE module in the stack comprises of an inner and outer silicon ring connected by thermocouples. The rings are, in essence, formed by etching away the silicon underneath the thermocouples during fabrication. The supporting membrane on the top of the thermopile serves as a mechanical connection between the silicon rings and also improves the structural stability of the device. Figure 2-7(A) shows the schematic of the stacked device; top and cross-sectional views of the individual TE modules are shown in Figure 2-7(B) and Figure 2-7(C) respectively.

Heat fins on the inner and outer silicon rings enhance the fluid-solid heat transfer, augmenting the temperature gradient across the thermopile. The inner silicon fins extrude longitudinally into the exhaust gas channel, while the outer annular fins enable cross-flow cooling. The outer annular fins are formed by making every fourth TE module in the stack to have a larger diameter.

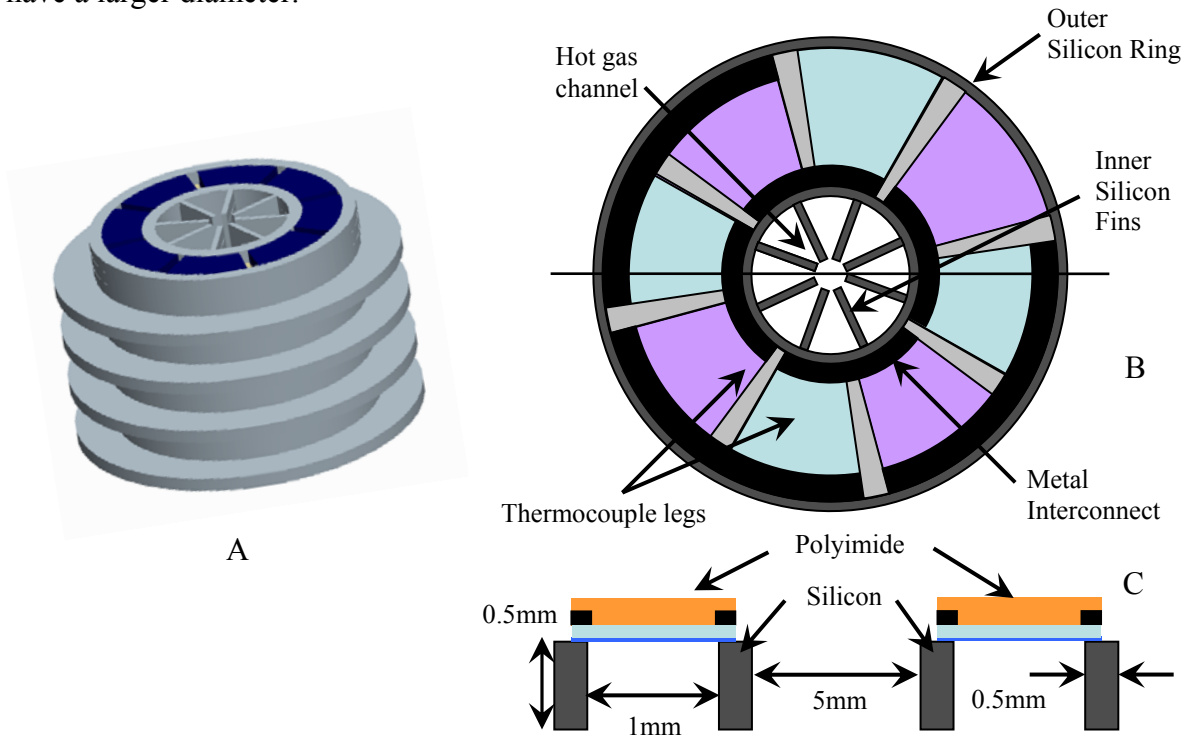


Figure 2-7. Stacked radial in-plane structure. A) Schematic view. B) Top view of a single radial in-plane TE module. C) Cross-sectional view of a single radial in-plane TE module.

This structure offers a good compromise between thermoelectric performance, fabrication complexity, and mechanical robustness. The absence of silicon underneath the thermopile greatly reduces thermal leakage. Additionally, by stacking of multiple modules, the output power is significantly enhanced as it is the sum of power generated by the individual modules. The stacking also results in a structure that is mechanically very stable. The circular shape of the center exhaust gas channel lends itself to easy fluidic coupling with the engine's exhaust outlet.

The fluidic resistance of the channel can be designed to be low enough as it is not limited anymore by wafer thickness.

Owing to the various advantages of the radial in-plane design, it is chosen as the structure for the TEG to be built. In the following sections, design parameters and the thermal modeling of the radial in-plane TEG are discussed in detail.

2.3 Device Design

Device design involves choice of materials, identification of key design parameters and determination of various device dimensions while meeting all the requirements outlined in Section 2.2. For the heat exchanger device, the most important design parameter is the maximum output power P_{out} that can be achieved when integrated with a thermopile. From Equations 2-1 and 2-2, it becomes essential that $\Delta T = T_{hot} - T_{cold}$ be increased for maximum P_{out} .

A simple expression for ΔT can be developed from the first-order analytical heat transfer model for stacked radial in-plane TEG. Since the stack is made up of several TE modules that are schematically the same, the thermal model of a single TE module would suffice for analysis. The thermal circuit model of the radial in-plane TE module is shown in Figure 2-8. Here, 1-D radial heat transfer is assumed, and end effects at the top and bottom of the stack are ignored. It can be seen that the model is generally the same as that of the simple in-plane TEG except that θ_{SiRing} replaces θ_{Si} . Obviously the individual thermal resistance values are slightly different.

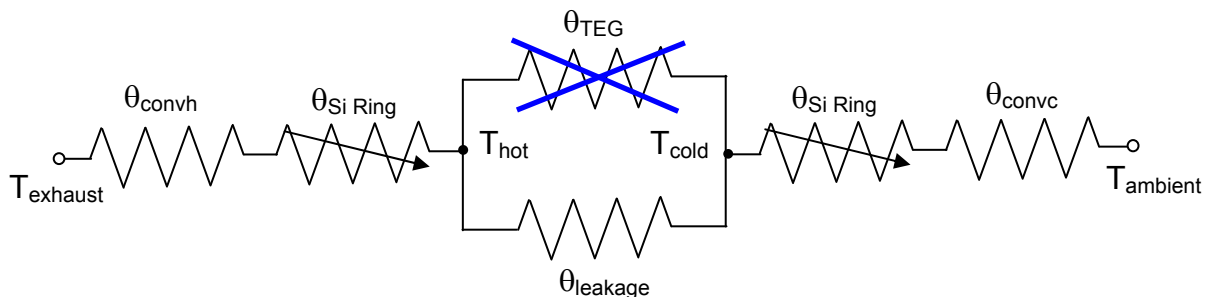


Figure 2-8. First-order equivalent thermal circuit of a radial in-plane TE module.

The thermal resistance component corresponding to the silicon rings, θ_{SiRing} is negligible due to the large surface area, short distance, and relatively high thermal conductivity of Si, and hence can be eliminated. θ_{convh} and θ_{convc} represent the convective thermal resistances on the inner and outer silicon rings respectively. θ_{TEG} is the effective conduction thermal resistance of the thermocouple legs and $\theta_{leakage}$ corresponds to the thermal leakage through the supporting membrane. It should be noted that since the aim of this research work is to demonstrate only a heat exchanger device, thermocouple legs will not be included in the design. Therefore, θ_{TEG} is eliminated from the thermal model. Nevertheless, expression for θ_{TEG} , and how it affects the thermal performance of the final device are presented for the sake of completeness. The temperature difference across the annular thermopile, $\Delta T = T_{hot} - T_{cold}$ is given by

$$\Delta T = \frac{(\theta_{TEG} \parallel \theta_{leakage})(T_{hfluid} - T_{cfluid})}{\theta_{convh} + \theta_{convc} + (\theta_{TEG} \parallel \theta_{leakage})}. \quad (2-8)$$

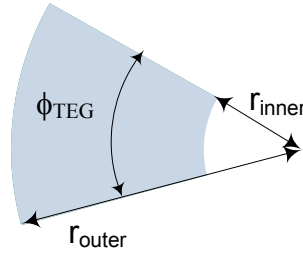


Figure 2-9. Dimensions of a single radial thermocouple leg.

The discussion in Section 2.2 regarding increase in ΔT with change in different thermal resistances applies to the radial in-plane design as well. Nevertheless, unlike in the in-plane design, θ_{TEG} and $\theta_{leakage}$ now represent thermal resistance to 1-D radial heat conduction [7]. θ_{TEG} can be expressed as

$$\theta_{TEG} = \frac{1}{n} \left(\frac{\ln(r_{outer}/r_{inner})}{\phi_{TEG} t_{TEG} k_{TEG}} \right) \quad (2-9)$$

where, r_{outer} and r_{inner} are the outer and inner radii of the radial thermocouple legs, ϕ_{TEG} is the angle subtended by the thermocouple leg at the center. Figure 2-9 shows the corresponding dimensions. Also, t_{TEG} is the thickness of the thermocouple leg, k_{TEG} is the thermal conductivity of the thermocouples, and n is the number of thermocouples.

$\theta_{leakage}$, on the other hand, is given by

$$\theta_{leakage} = \left(\frac{\ln(r_{outer}/r_{inner})}{2\pi t_{mem} k_{mem}} \right). \quad (2-10)$$

where, t_{mem} and k_{mem} are the thickness and thermal conductivity of the annular supporting membrane.

In the following subsections, details are presented on how the device dimensions are chosen based on the simple thermal model of Figure 2-8.

2.3.1 Fin Geometry Optimization

The convective thermal resistance of the inner and outer ring surfaces is given by Equation 2-4 and is repeated here for convenience.

$$\theta_{conv} = \frac{1}{hA_s} \quad (2-7)$$

As shown in Figure 2-7(B), the inner ring surface of the radial TE module is longitudinally finned to achieve higher convection surface area A_s . But when A_s is increased arbitrarily, say by increasing the number of fins, the fluid flow through the center channel is constricted, reducing the flow velocity and hence the convective heat transfer coefficient h [7]. Therefore,

the fin geometry – number and dimensions of the fins, have to be optimized for lowest convection thermal resistance.

The heat transfer coefficient, h , by definition, is an empirical parameter, and so any optimal solution for low θ_{conv} can be achieved only based on experimental data. Fin correlations for a variety of fin geometries and channel configurations exist in literature [27], [28]. For the radial in-plane TE module, optimization of the inner ring longitudinal fins was accomplished using correlations for internally finned tubes obtained by Hu and Chang [27]. These correlations list the Nusselt's numbers and friction factor-Reynold's number products for different number of fins and different lengths in circular ducts.

Before the actual fin optimization is presented, a few important terms are defined:

(A) Friction factor, f – it is a dimensionless quantity given by the expression

$$f = \frac{\tau_s}{\rho u_\infty^2}, \quad (2-11)$$

where, τ_s is the surface shear stress on pipe walls, ρ is the density of the fluid, u_∞ is the free stream fluid velocity. It can also be shown that the friction factor is directly proportional to the pressure gradient needed to sustain the flow. Therefore, for the center channel of the radial TE device, a high friction factor would be undesirable as it would exert backpressure on the exhaust outlet of the combustion engine.

(B) Nusselt's number, Nu – this is defined as the dimensionless temperature gradient at the convective surface of interest, and given by the expression

$$Nu = \frac{hD}{k}, \quad (2-12)$$

where, h is the convection heat transfer coefficient, D is the diameter of the channel, and k is

the thermal conductivity of the fluid. As is obvious, a high Nu implies high h and is needed to achieve low θ_{conv} .

From the correlation data, friction factors and heat transfer coefficients are determined assuming a fully developed laminar flow (Reynold's number, $Re = 1.53 \times 10^3$) of air in a finned channel of diameter 3 mm. The fully-developed laminar flow assumption is likely not satisfied in the actual design, but this serves as a starting point for the design. The thermal conductivity of air, $k = 0.0323 \text{ W/m}\cdot\text{K}$ is used for the calculations. The computed values are plotted against number of fins for different fin lengths (Figure 2-10).

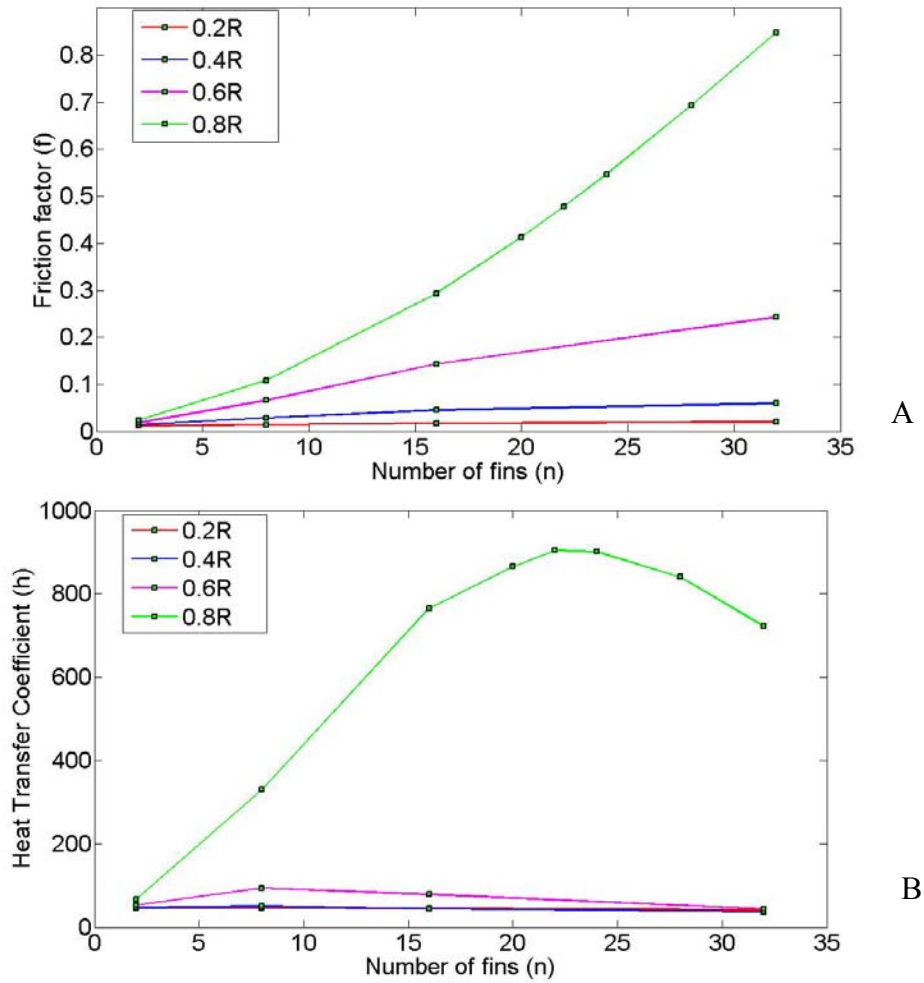


Figure 2-10. Fin geometry optimization. A) Plot of Friction factor Vs Number of fins. B) Plot of Heat transfer coefficient Vs Number of fins for different fin lengths.

The plots in Figure 2-10 show that with a fin length, $l = 0.8R$, high values of h could be achieved as n is increased. However, for any number of fins above $n = 8$, the friction factor becomes prohibitively large. Thus, a length, $l = 0.8R$ and $n = 8$ were chosen for the longitudinal fins on the inner ring.

To achieve a low θ_{conv} , annular fins are formed on the outer side by inserting a TE module with a larger outer diameter every fourth module in the stack. In the final structure, this creates an annularly finned outer shell, where the fins are highly conductive silicon. The advantage of annular fins as compared to longitudinal fins on the outer side is fabrication simplicity. Moreover, the cross-flow cooling would likely be transverse to the exhaust gas flow in an actual system, e.g. small combustion engine. Unlike the longitudinal fins on the inner ring, the dimensions of the annular outer fins are not optimized but simply selected. A fin length of 2 mm is chosen to provide a reasonable aspect ratio (the fin thickness is the wafer thickness of 300-500 μm) without creating excessively large modules. Large dies require more area on the silicon wafer and thus limit the number of devices that can be fit on a given substrate for microfabrication.

2.3.2 Exhaust Gas Channel Design

The diameter of the center exhaust gas channel needs to be large enough to meet the low fluidic resistance requirement. To this end, a model airplane engine is selected as a candidate exhaust gas device and characterized to determine the maximum fluid backpressure that it can withstand. The experiment is done by blocking the exhaust outlet of the engine with a metal piece containing a circular hole. The procedure is repeated with smaller hole diameters until the engine starts choking. It was found that the engine started choking for hole diameters less than 5 mm. Therefore, the diameter, d , of the exhaust gas channel is chosen as 5 mm.

2.3.3 Ring Thickness and Space between Rings

The only constraint for the inner and outer Si rings is that they should be wide enough for the TE module to be structurally strong. Due to its high thermal conductivity, the thermal resistance of the Si rings is negligible. Based on these considerations, the ring width is chosen as 0.5 mm. It should be noted that for the larger TE modules that form the annular outer fin, the outer ring width is 2.5 mm. The inner ring width is 0.5 mm for both TE modules.

Referring to Figure 2-7(B), thus far, all the device dimensions are fixed except for the distance between the silicon rings. If the distance between the rings is assumed to be s , then the overall radius of the smaller TE module can be written as below:

$$R = \frac{d}{2} + 2t_{ring} + s \quad (2-13)$$

where, R is the overall device radius, d is the diameter of exhaust gas channel, t_{ring} is the Si ring thickness and s the space between the rings. By limiting the maximum overall device diameter to 10 mm (excluding the outer fins), the maximum device radius is set to $R_{max} = 5$ mm.

Rewriting Equation 2-13 to determine the maximum space between the rings s_{max} ,

$$s_{max} = R_{max} - \frac{d}{2} - 2t_{ring} \quad (2-14)$$

$$\Rightarrow s_{max} = 1.5 \text{ mm}$$

Thus the silicon rings can be anywhere from 0 – 1.5 mm apart. While determining an optimized value of s demands the knowledge of thermopile design (thermocouple leg dimensions and material properties), a reasonable value for s can be chosen based on simple analysis.

A small value of s yields only low thermal resistances θ_{TEG} and $\theta_{leakage}$. This can be illustrated easily by recalling the expressions for θ_{TEG} and $\theta_{leakage}$ from Equations 2-9 and 2-10.

Repeating θ_{TEG} here for convenience,

$$\theta_{TEG} = \frac{1}{n} \left(\frac{\ln(r_{outer}/r_{inner})}{\phi_{TEG} t_{TEG} k_{TEG}} \right) \quad (2-9)$$

For the thermocouple legs which contributes θ_{TEG} and the supporting membrane which contributes $\theta_{leakage}$, the space between the rings, s corresponds to the difference between r_{outer} and r_{inner} ,

$$s = r_{outer} - r_{inner} \quad (2-10)$$

Since r_{inner} is set when the radius of the exhaust gas channel is fixed, decreasing s results in a small r_{outer} and hence low θ_{TEG} . The same argument is applicable to $\theta_{leakage}$ also. Therefore, shorter distance between silicon rings degrades ΔT and P_{out} .

On the other hand, when s is on the higher side, ΔT will be large but at the cost of increased electrical resistance R_{elec} , resulting in a lower P_{out} . With increased distance between the rings, the device would also be mechanically weaker. Based on the trade-offs discussed here, the distance between the silicon rings is chosen to be 1 mm.

Lastly, the properties of the supporting membrane need to be mentioned. As it forms the only the leakage path between the hot and cold sides, the membrane should have low thermal conductivity. It should also offer sufficient mechanical strength to support the thermocouples and to hold the two silicon rings together. Photodefinable polymer epoxies form potential candidates for this purpose, as the deposition and patterning steps can be seamlessly integrated

into the heat exchanger process flow. Details regarding material selection and necessary process steps to integrate the supporting membrane are discussed in Chapter 3.

2.4 Thermal Modeling

In the previous section, a simple first-order heat transfer model is presented to gain insight into the different performance trade-offs and to choose heat exchanger device dimensions. However, the model may not be adequate enough to accurately predict the ΔT that would be generated for a given exhaust temperature. With this objective, a more detailed thermal model is developed in this section.

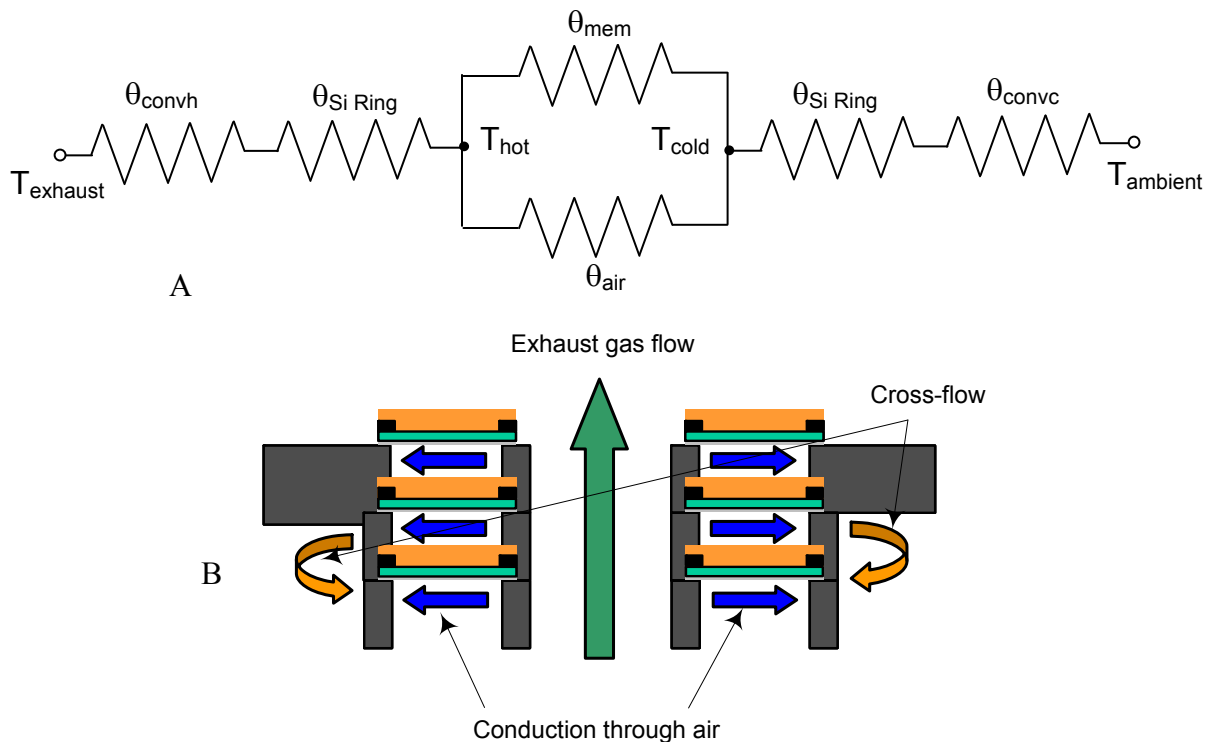


Figure 2-11. Detailed thermal model of radial in-plane structure. A) Thermal equivalent circuit of the radial in-plane heat exchanger module. B) Cross-sectional view of the heat exchanger stack showing different thermal paths.

Figure 2-11(A) shows the detailed thermal model. The additional component that is modeled here is the conduction thermal path through air between the silicon rings, depicted in Figure 2-11(B). The conduction resistances of the inner and outer silicon rings are also considered. In what follows, expressions for each thermal resistance component in the model of

Figure 2-11(A) are presented. The equations for conduction thermal resistances θ_{TEG} and θ_{mem} , have already been presented; θ_{air} can also be expressed in a similar fashion. All the three are listed for the sake of completeness.

$$\theta_{TEG} = \frac{1}{n} \left(\frac{\ln(r_{outer}/r_{inner})}{\phi_{TEG} t_{TEG} k_{TEG}} \right) \quad (2-9)$$

$$\theta_{mem} = \left(\frac{\ln(r_{outer}/r_{inner})}{2\pi t_{mem} k_{mem}} \right) \quad (2-10)$$

$$\theta_{air} = \left(\frac{\ln(r_{outer}/r_{inner})}{2\pi t_{air} k_{air}} \right) \quad (2-15)$$

where, r_{outer} and r_{inner} are the outer and inner radii of the radial thermocouple legs, ϕ_{TEG} is the angle subtended by the thermocouple leg at the center, k and t represent the thicknesses and thermal conductivities of the respective materials. In all previous discussions, the thermal conductivities of different materials are assumed to be constant. In reality, the thermal conductivities do change with temperature and the temperature dependence of k for standard materials can be found in literature [7]. This variation in k needs take into account when computing the thermal resistances listed above.

Next, the convection thermal resistances are given by

$$\theta_{convh} = \frac{1}{h_h A_{s,h}}, \text{ and} \quad (2-16)$$

$$\theta_{convc} = \frac{1}{h_c A_{s,c}}. \quad (2-17)$$

where, h_h and h_c are the convection heat transfer coefficients for longitudinal flow on the inner channel and cross-flow over the outer ring respectively; similarly, $A_{s,h}$ and $A_{s,c}$ represent

convection surface areas on the hot and cold sides. As the inner fin design is based on empirical correlations, the heat transfer coefficient, h_h can directly obtained from the correlations.

Empirical data indicate that for a fin length, $l = 0.8R$ and number of fins, $n = 8$, the Nusselt's number, Nu is 30.65 [27]. h_h can be obtained by rearranging Equation 2-12.

$$h_h = \frac{k_{air} Nu}{D_{inner}} \quad (2-18)$$

where, k_{air} is the thermal conductivity of air, again a function of temperature, and D_{inner} is the diameter of the center channel.

To compute the convection coefficient, h_c for the outer ring, two different cases need to be considered – with and without external cross-flow. Again, standard textbook correlations to compute Nu are available for both natural and forced cross-flow convection over long cylinders. From Nu values, h_c can be obtained using Equation 2-12. For the sake of simplicity, annular fins on the outer side are ignored.

From Incropera [7], the expression for Nusselt number for free convection around a horizontal cylinder is given by

$$Nu = \left\{ 0.6 + \frac{0.387 Ra^{1/6}}{\left[1 + \left(0.559 / Pr \right)^{9/16} \right]^{8/27}} \right\} \quad (2-19)$$

where, Ra and Pr represent the Rayleigh and Prandtl numbers for air around the cylinder calculated a given temperature. These are given by

$$Ra = \frac{g \beta (T_{cold} - T_{ambient}) D_{outer}^3}{\nu \alpha}, \text{ and} \quad (2-20)$$

$$Pr = \frac{\nu}{\alpha} . \quad (2-21)$$

where, g is acceleration due to gravity, T_{cold} is the outer ring temperature, $T_{ambient}$ is the ambient temperature, and D_{outer} is the diameter of the outer ring. β , ν , and α are fluidic properties of air, that are generally dependent only on temperature.

β is called the volumetric thermal expansion coefficient of the fluid and determines how density of the fluid changes with temperature. ν is called kinematic viscosity and is simply the ratio of the absolute viscosity of the fluid to its density. Lastly, α is called thermal diffusivity, defined as the ratio of thermal conductivity to heat capacity of the fluid.

Nusselt's number for cross-flow over a cylinder is a function of the flow velocity. Using correlation suggested by Churchill and Bernstein [7], Nu for cross-flow case is given by

$$Nu = 0.3 + \frac{0.62Re^{1/2}Pr^{1/3}}{\left[1 + \left(0.4/Pr\right)^{2/3}\right]^{1/4}} \left[1 + \left(\frac{Re}{282000}\right)^{5/8}\right]^{4/5} \quad (2-22)$$

where Re is the Reynold's number for the cross-flow and Pr is the Prandtl number for air. Re can be obtained using

$$Re = \frac{V_{cross-flow} D_{outer}}{\nu} . \quad (2-23)$$

The analytical model just described was implemented in MATLAB, and T_{hot} , T_{cold} and ΔT for a range of exhaust gas temperatures, $T_{exhaust}$ were estimated. The temperature dependence of the fluidic properties such as β , ν , and α is accounted for by calculating their values for each $T_{exhaust}$. The results predicted by the MATLAB model is later used to compare with experimentally obtained values.

2.5 Final Dimensions of the Radial In-plane TE Modules

Figure 2-12 shows the device dimensions for the small and large heat exchanger modules that need to be fabricated. As can be seen, the thickness of outer Si ring is the only difference between the two modules. The thickness of both the modules is just the thickness of a standard silicon wafer (300-500 μm).

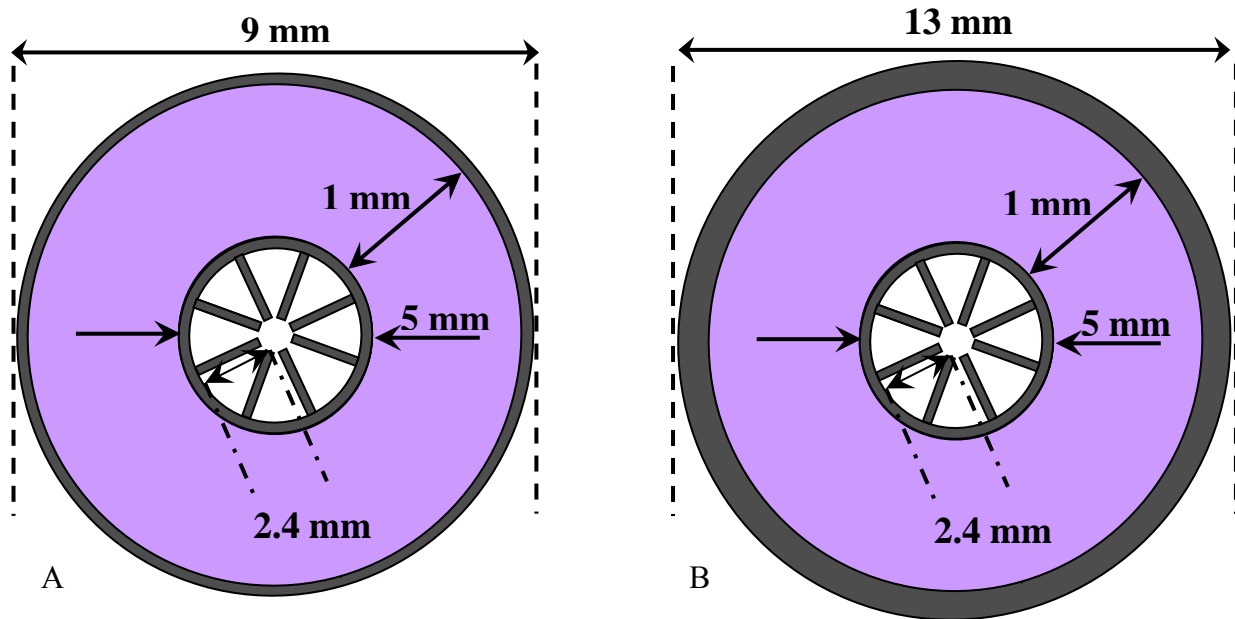


Figure 2-12. Final device dimensions. A) Small TE module. B) Large TE module with wider outer Si ring.

2.6 Summary

In this chapter, all aspects of heat exchanger device design were discussed. The performance requirements were identified, and based on that, different device structures were evaluated. The stacked radial in-plane design was chosen as the structure to be fabricated. With the aid of a first-order heat transfer model, the device dimensions were established considering various design trade-offs. Also, a detailed thermal model was developed to predict the thermal isolation performance of the designed heat exchanger.

CHAPTER 3 FABRICATION AND STACKING OF THE HEAT EXCHANGER MODULES

This chapter discusses in detail the process steps involved in fabricating the individual heat exchanger unit modules and how the modules are stacked. As discussed in Chapter 2, the thermal leakage between the hot and cold sides of the heat exchanger should be as small as possible for the heat exchanger to be most efficient. This necessitates removal of all the silicon underneath the thermocouples thereby restricting the thermal path primarily to the thin polyimide membrane. The resultant device has two concentric Si rings connected by the polyimide membrane. The cross-section of the unit heat exchanger module is shown in Figure 3-1.

3.1 Through-Etching of Wafers

Removal of bulk silicon underneath the thermopile implies that the wafer needs to be etched through its entire thickness of around 500 μm to 600 μm . A high etch rate is therefore essential to avoid excessive process time. Also, a high degree of anisotropy is desired to realize a center exhaust channel of uniform diameter. Options for anisotropic etch of bulk silicon include wet etching techniques such as the KOH based etch or dry etching techniques such as the plasma based reactive ion etching (RIE) and deep reactive ion etching (DRIE). However, because of its high etching speed, better anisotropy, vertical side-wall profile and ease of wafer handling, Bosch's DRIE technique [29] becomes the obvious choice.

The DRIE process utilizes alternate etch and passivation cycles to achieve high anisotropy. During passivation, a chemically inert compound similar to Teflon is coated on side-walls to prevent undercutting. Typically, the etch and passivation cycles last several seconds, and the fine balance between durations of each cycle is what determines

the side-wall profile. The technique uses SF_6 and O_2 during the etch cycle and C_4F_8 for the passivation cycle [30]. For heat exchanger device fabrication, etching is performed using Surface Technology Systems' (STS) Multiplex ICP ASE (Inductively Coupled Plasma Advanced Silicon Etcher).

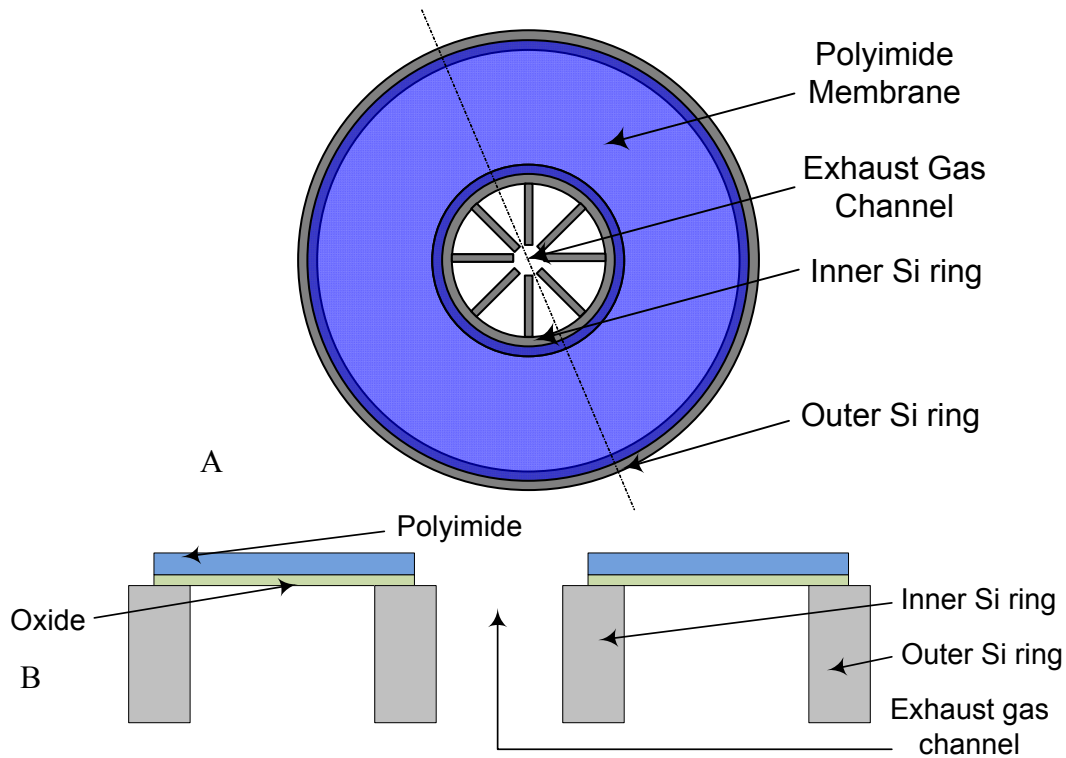


Figure 3-1. Heat exchanger module to be fabricated. A) Top View B) Cross-sectional view

3.2 Membrane Strength Evaluation

HD Microsystems' product HD-8820 Aqueous Positive Polyimide [31] is chosen as the material for the membrane connecting the Si rings. It offers good mechanical strength, low thermal conductivity, and temperature compatibility up to $450\text{ }^\circ\text{C}$. In addition, its photodefinability is used to pattern the membrane without the need for photoresist and thereby reducing the number of process steps. The polyimide membrane thickness is a critical parameter in the design of the heat exchanger. A thin membrane would offer low thermal leakage, but the resulting device may not be structurally stable.

On the other hand, a thick membrane would compromise the thermal isolation of the heat exchanger. For this reason, the optimum polyimide thickness is found by trial and error; multiple devices are fabricated with different polyimide thicknesses – 5 μm and 10 μm of HD8820. Although both devices are mechanically robust, some devices with 5 μm polyimide had issues like cracks and membrane peel-off. However, through fine control of the number of DRIE cycles and careful handling of the devices during final release, an overall yield of more than 90% could be achieved. Thus, the thinner 5 μm is chosen as the polyimide thickness.

3.3 Process Flow Description

The heat exchanger process flow is devised with the target thermoelectric generator (TEG) in mind so that process steps pertaining to thermopile fabrication can be readily accommodated (in future builds). Table 3-1 lists all the processing steps in detail, and Figure 3-2 shows the device cross-sections at each step. The process starts with a double side polished (DSP) (100) 100-mm Si wafer of thickness 500 μm with 300 nm of thermal oxide on both sides. A 5 μm thick polyimide layer is deposited, patterned and cured on the front-side. This layer acts as the supporting membrane for the thermoelectric elements in the TEG. The exposed thermal oxide on the front-side and the oxide layer on the back-side are removed using 6:1 buffered oxide etch (BOE). The front-side oxide layer mimics the buffer layer required in future builds to grow the thermoelectric PbTe thermoelements. It also plays the role of etch stop during the final DRIE step. After the oxide removal, photoresist is spun on the back-side and patterned after front-to-back alignment using EVG[®] 620 Precision Mask Aligner. The wafer is then attached to a handle wafer using AZ9260 photoresist, and back-side through-wafer DRIE is performed. This step removes the bulk silicon under the thermopile, creates the central aperture, and

forms an inner and an outer silicon ring. In addition, the DRIE step singulates the individual heat exchanger modules, but they remain attached to the handle wafer. The modules are released from the handle wafer in an acetone bath that also removes the photoresist on the back-side.

Square shaped longitudinal fins are formed on the inner silicon ring, also during the DRIE step; patterns for these are included in the back-side mask. On the other hand, outer silicon rings are formed during the stacking process presented in Section 3.5. Initially, square shaped unit modules with longitudinal inner and outer fins were fabricated. The dimensions of this square device were similar to the circular shaped devices. These square devices served as a test vehicle to evaluate the process flow, and fix process parameters such as the DRIE chamber pressure and gas flow rates.

Table 3-1. Heat Exchanger Process Flow.

Step	Process Description
1	Start with double side polished (DSP), <100> crystal orientation, n-type Si wafers with 300nm thermal oxide on both sides
2	Spin deposit a 5µm thick polyimide (HD8820) layer on the front-side
3	Pattern and cure polyimide layer
4	Remove exposed front-side oxide and back-side thermal oxide through a 6:1 BOE
5	Deposit and pattern 10µm thick AZ5260 photoresist on back-side after front-to-back alignment
6	Attach handle wafer on the front-side using AZ9260 photoresist
7	DRIE back-side to form the central aperture and the Si rings
8	Release heat exchanger modules by removing photoresist in acetone bath

3.4 Mask Making

Heat exchanger module fabrication requires only two photomasks – one for patterning the front-side polyimide and another for the back-side through-wafer etch. The masks are designed using AutoCAD 2008 (Figure 3-3). These masks are printed using emulsion on polyester films at J.D. Photo Tools, U.K. The mask patterns are later

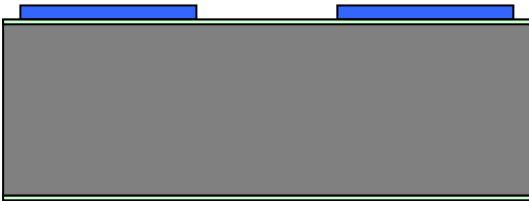
a) Start with DSP Si wafers with 300nm thermal oxide on both sides



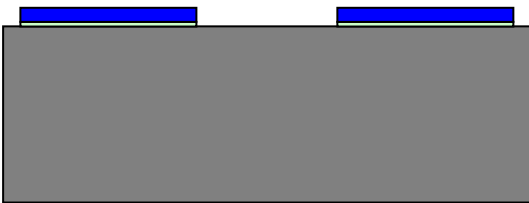
b) Deposit HD8820 polyimide



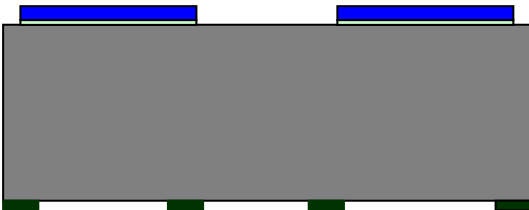
c) Pattern polyimide



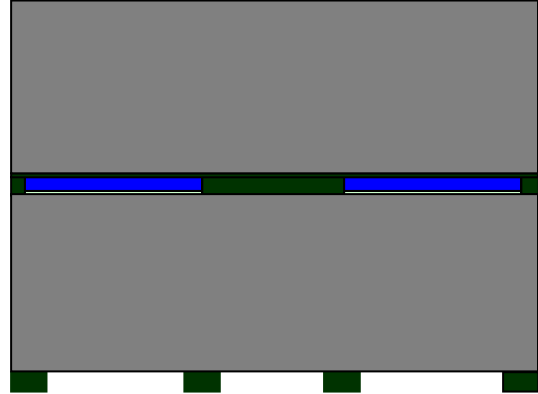
d) Remove thermal oxide through BOE



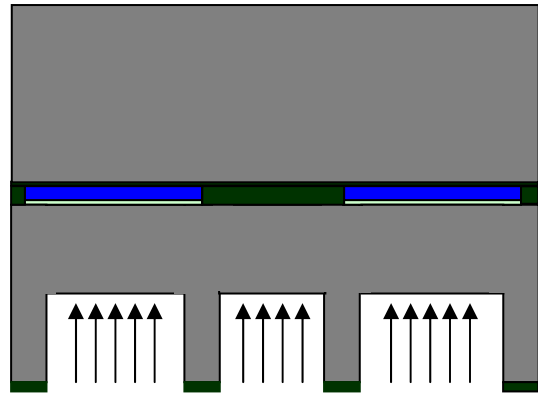
e) Deposit photoresist on back-side



f) Attach handle wafer on the front-side with AZ9260 photoresist



g) Through-wafer DRIE from back-side



h) Release heat exchanger modules in acetone bath

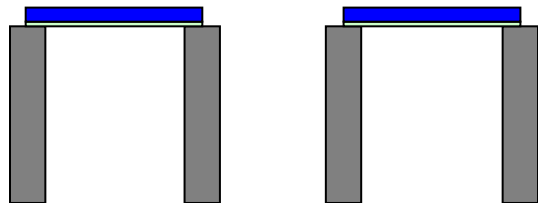


Figure 3-2. Device cross-sections during various process steps.

transferred on to 5" x 5" chrome/soda lime glass plates using MA6 Mask Aligner. These glass plates serve as the master-masks used in patterning of photoresist and polyimide.

Both masks have patterns for fabricating 12 large modules of 13 mm diameter and 36 small modules of 9 mm diameter, yielding enough devices to make two 12 mm long tubular thermoelectric generators. Certain heat exchanger modules are designed with access windows of 5.6 mm on the outer Si ring to enable temperature measurements using external thermocouples. An array of alignment marks is added in the mask to facilitate easy front-to-back alignment. Also, the back-side mask patterns are designed to match with the mirror image of the front side patterns to account for the wafer flipping involved in front-to-back processing.

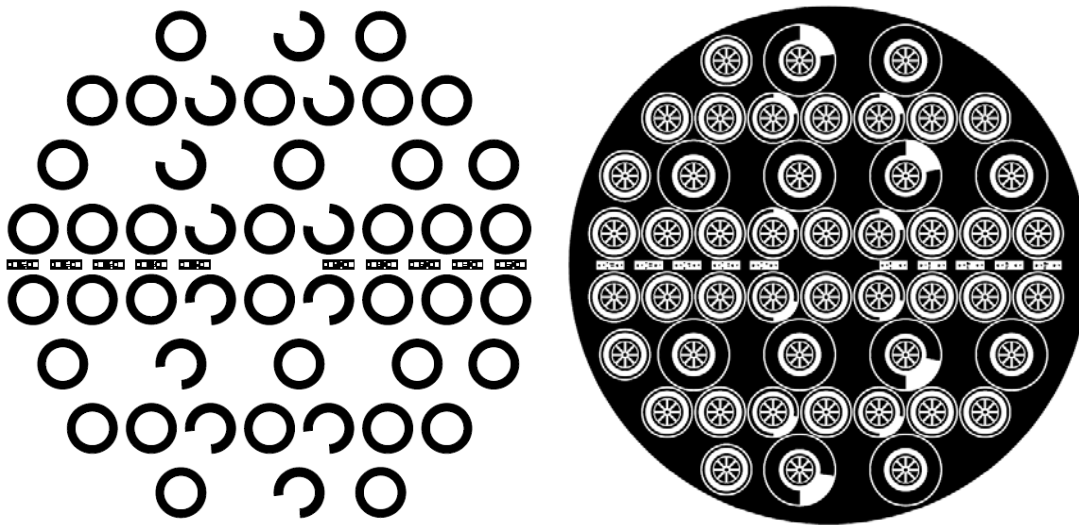


Figure 3-3. Mask patterns. A) Front-side mask pattern. B) Back-side mask pattern.

3.5 Stacking and Bonding of Heat Exchanger Unit Modules

The singulated heat exchanger modules are stacked and bonded to form the tubular heat exchanger. Stacking is done using a simple assembly jig with two parallel metal rods that are spaced precisely to match the device dimensions. Figure 3-4 shows both a top view and a photograph of the stacking setup. The diameter of the rods is accurately chosen so that it fits closely between two opposite pairs of inner fins of the heat exchanger module. The individual

modules are slid one by one over the alignment rods while a thermally conductive epoxy is applied on each module to facilitate bonding. The annular outer fins are formed by inserting one large (13 mm) module for every three small (9 mm) modules.

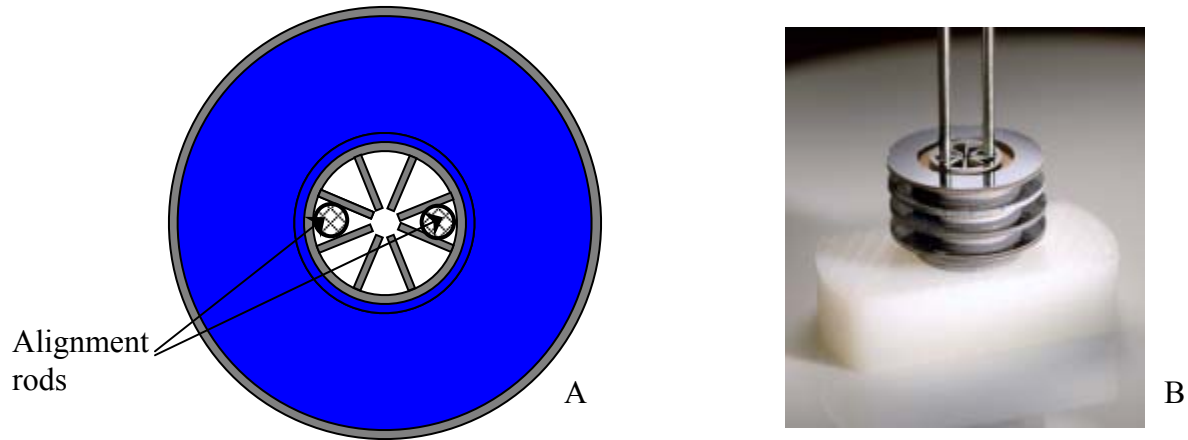


Figure 3-4. Assembly jig. A) Schematic top view. B) Photograph.

Two different thermally conductive epoxies are tried in attempts to bond the individual modules. First, a Pb-Sn based solder epoxy (Figure 3-5(A)), is deposited in tiny droplets around the periphery of the inner and outer Si rings. The deposition is done using EFD[®] Fluid Dispenser and the droplet size is fixed at 100-150 μm using appropriate dispensing tips. The stacked device is then cured in an oven at 200 °C. After curing, the device is structurally strong at room temperature; however it is experimentally found that bonding between the individual modules weakened at temperatures above 250 °C.

The second bonding method is attempted using a high temperature epoxy (Figure 3-5(B)) from J-B Weld; the epoxy is made by mixing equal parts of two different pastes – liquid steel epoxy resin and a hardener. The mixture is applied carefully around the inner and outer Si rings on each heat exchanger module as they are stacked. Figure 3-6 shows the application method employed for each kind of epoxy. Curing is done at room temperature over a period of 24 hours.

The cured device is found to be mechanically robust even at temperatures close to 400 °C. Therefore, this epoxy is chosen to bond the modules of the actual heat exchanger device.



Figure 3-5. Epoxies for bonding heat exchanger modules. A) Solder epoxy from EFD. [Adapted from <http://www.efd-inc.com/Solder/Dispensing>] B) High-temperature epoxy from JB Weld. [Adapted from <http://www.jbweld.net/products/jbweld.php>]

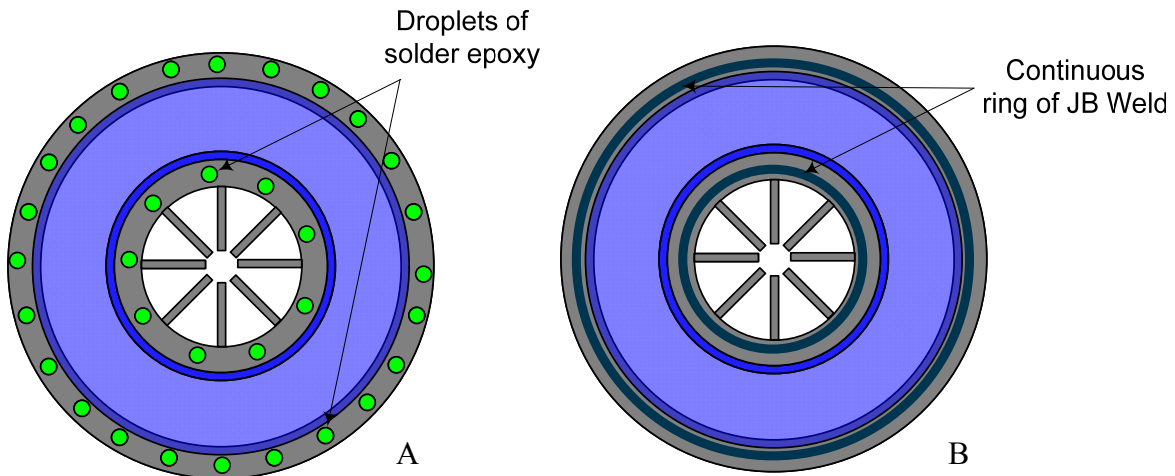


Figure 3-6. Epoxy application methods. A) Solder epoxy. B) High temperature epoxy (JB Weld).

After curing, the stack possesses a sealed inner channel for the passage of the hot exhaust gas with longitudinal fins extending into it. The thermally conductive nature of the epoxy enables thermal conduction between the rings in the vertical direction. This helps maintain a uniform inner ring temperature and a uniform outer ring temperature along the length of the tubular device.

3.6 Final Device Photographs

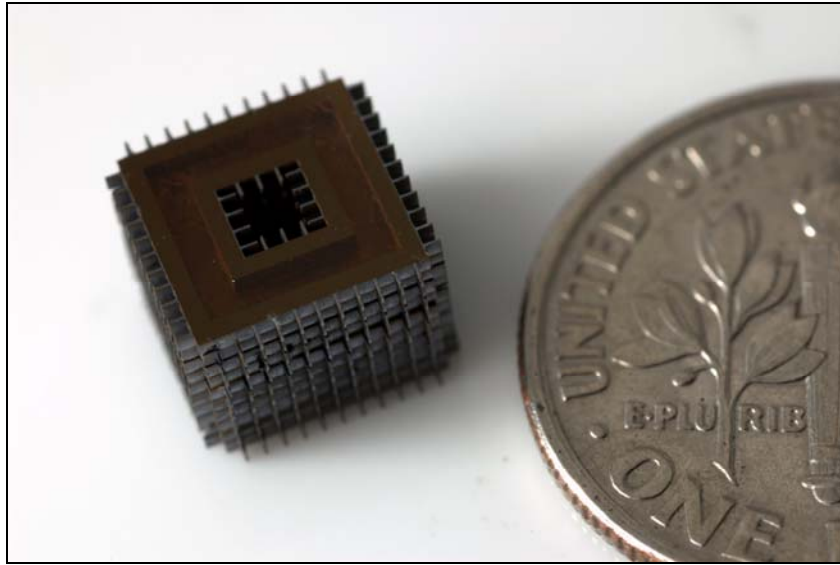


Figure 3-7. Heat exchanger stack built with square shaped modules.

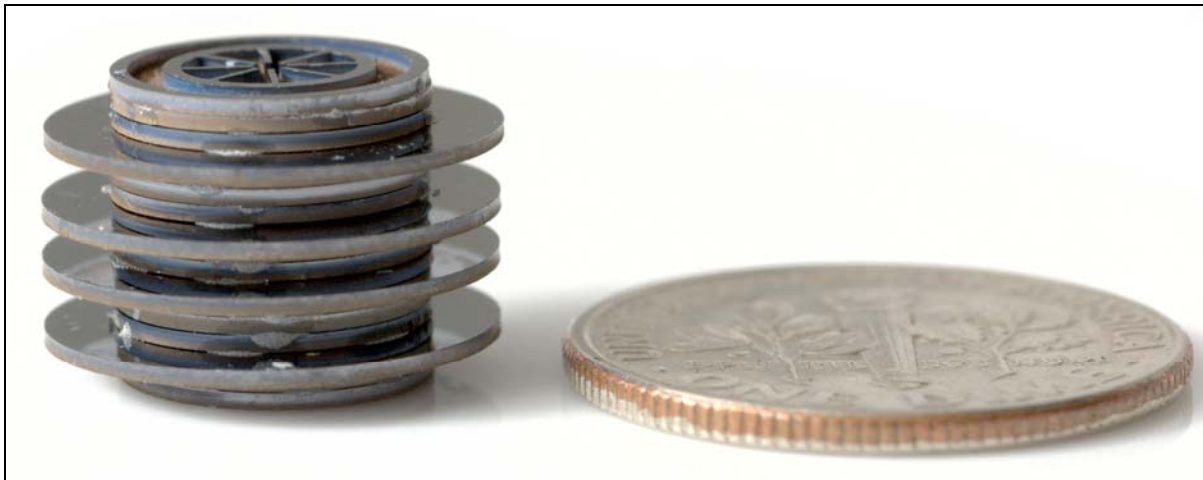


Figure 3-8. Heat exchanger built with circular modules.

3.7 Summary

The proposed heat exchanger device was built by fabricating and stacking individual TE modules. For TE module fabrication, polyimide was chosen as the supporting membrane, and DRIE was used to remove bulk silicon and form the center exhaust channel. The modules were stacked using a simple assembly setup, while bonding was achieved using a high temperature epoxy from JB Weld.

CHAPTER 4 CHARACTERIZATION OF THE HEAT EXCHANGER DEVICE

In this chapter, the experimental setup and procedure used to characterize the stacked radial in-plane heat exchanger device are described. Following this, the test results obtained from the experiments are presented in various graphs and tables; the results are also compared with the theoretical model predictions. The chapter concludes with a discussion on the limitations of the test procedure, and reasons for deviation of the experimental results from theoretical results.

4.1 Experimental Setup and Procedure

Tests are performed on the heat exchanger device to characterize the thermal isolation – temperature difference, $\Delta T = T_{hot} - T_{cold}$, that is created between the inner hot Si ring and the outer Si ring for various temperatures and velocities of hot gas flowing through the center channel. Sustaining a high ΔT temperature across the thermocouple legs in the final TEG is critical for power generation.

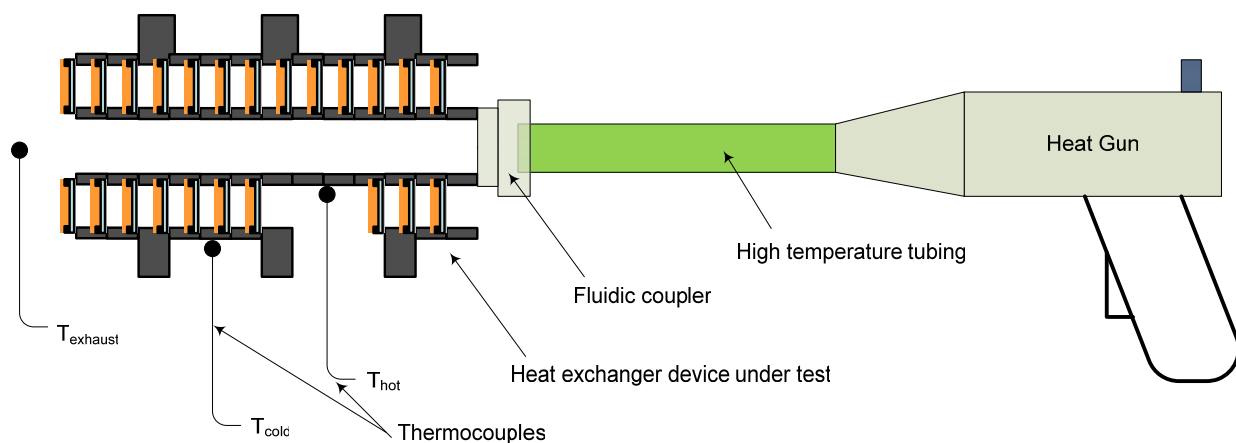


Figure 4-1. Experimental setup to test the heat exchanger device.

The schematic of the experimental setup is shown in Figure 4-1. A commercially available hot air gun is used as the source of hot gas; the outlet of the heat gun is connected to the sealed

inner gas channel of the heat exchanger under test through high temperature tubing and appropriate fluidic couplers. Master Appliance's Proheat[®] Variair Heat Gun, PH-1300 [32] is used for this purpose; the variable temperature, variable air flow rate capability of the heat gun enables device testing under different conditions. The shrink tubing attachment is used to confine the hot air flow only to the connecting tube; moreover, the connecting tube is glued to the heat gun outlet to prevent detachment during the experiment. Prior to the experiment, an aluminium fluidic coupler is bonded to the stacked heat exchanger using the high temperature epoxy, J-B Weld. Figure 4-2 shows the heat exchanger device with the fluidic coupler bonded at the bottom end. The coupler is machined accurately to make a snug fit with the connecting tube, thereby ensuring a leakage free conduit for the hot gas from the heat gun outlet to the center channel of the heat exchanger.



Figure 4-2. Heat exchanger device bonded with the fluidic coupler.

The device is tested under two different configurations – in the first, the outer ring is cooled only by natural convection while in the second, forced convection is used for cross-flow cooling of the outer ring. In both cases, the inner silicon ring is heated by the hot air from heat gun. The cross-flow for the forced convection tests is created by a miniature fan, positioned to provide a fairly uniform flow around the device. As part of the experiment, the temperature of

the hot air through the center channel, $T_{exhaust}$, velocity of the hot air, $V_{exhaust}$ and the cross-flow velocity, $V_{cross-flow}$ are changed, and temperatures of the inner and outer Si ring, T_{hot} and T_{cold} , are measured. The tools and methods employed to measure these experimental parameters are described in the sub-sections that follow.

4.1.1 Flow Measurements

A hot-wire anemometer is used to measure the velocity of the hot air and that of the cross-flow. Hot-wire anemometry involves exposure of an electrically heated element probe to a fluid medium in order to measure the medium properties such as velocity and composition. For the heat exchanger experiments, a constant temperature anemometer (CTA) with tungsten wire probe is used. The principle of operation of a CTA is to maintain a constant wire temperature using an internal negative feedback system comprised of a wheatstone bridge and a servo amplifier. The system schematic of the CTA is shown in Figure 4-3.

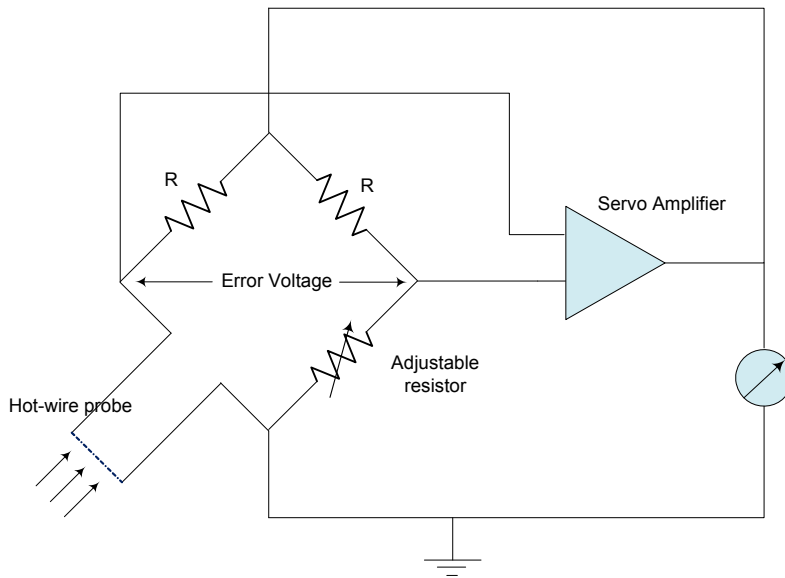


Figure 4-3. System schematic of a constant temperature anemometer.

When introduced into a fluid flow, the temperature of the wire drops due to convective cooling and consequently its electrical resistance decreases, due to the temperature coefficient of

resistance of the tungsten metal. This causes an imbalance in the bridge circuit creating a finite error voltage across the input terminals of the servo amplifier. The amplifier acts to counter the imbalance by forcing more current through the hot-wire, which, by virtue of joule heating increases the wire temperature. With increasing flow velocity, the error voltage and hence the amplifier output voltage both increase. Thus, the amplifier output serves as a direct measure of the fluid flow velocity.

In practical measurements, the fluid velocity is determined using King's law [33], which is given by

$$E^2 = A + Bu^n \quad (4-1)$$

where E is the analog output voltage of the CTA, u is the velocity of the flow normal to the wire; A , B , and n are constants. Before actual velocity measurements are performed, the hot-wire anemometer is calibrated to ascertain the constants A , B , and n in Equation 4-1. The calibration process involves exposing the hot-wire probe to a set of known velocities and noting the output voltages. The King's law calibration constants can then be calculated using a power-law curve fit on the calibration data.

During heat exchanger testing, as the temperature of the center channel hot-air is varied, the measured hot-wire anemometer output voltages need to be temperature corrected before computing flow velocities. The modified King's law with temperature correction is given by

$$\frac{E^2}{T_{wire} - T_{flow}} = A + Bu^n \quad (4-2)$$

where, T_{wire} is the hot-wire temperature, and T_{flow} is the temperature of the fluid flow. The hot-wire temperature, T_{wire} can be found using

$$T_{wire} = \frac{a}{\alpha_0} + T_0 \quad (4-3)$$

where T_0 is the reference ambient temperature during calibration, α_0 is the temperature coefficient of resistance (TCR) of the hot-wire probe at temperature T_0 , and a is a constant called overheat ratio that is established at the time of calibration. The ratio $\frac{a}{\alpha_0}$ is usually defined as the overtemperature and denoted by $T_{overtemp}$,

$$T_{overtemp} = \frac{a}{\alpha_0}. \quad (4-4)$$

Once the calibration constants A , B , and n and overtemperature, $T_{overtemp}$ are determined, the fluid velocity values can be obtained using the expression

$$u_{flow} = \sqrt[n]{\left(\frac{E_{flow}^2}{T_{wire} - T_{flow}} - A \right) / B}. \quad (4-5)$$

where E_{flow} is anemometer output voltage for a flow with velocity u_{flow} and temperature T_{flow} .

Table 4-1 lists in a step-by-step fashion all the steps involved in hot-wire calibration and flow velocity measurement. It should be added that for cross-flow velocity measurement, steps pertaining to temperature correction are not required as the flow temperature is the same as the ambient temperature.

Table 4-1. Flow velocity measurement procedure using the CTA.

Step	Description
1	Calibrate the hot-wire probe by forcing air streams of known velocities, u and measure CTA output voltages E .
2	Measure the ambient temperature during calibration process. This forms the reference temperature, T_0 .
3	Determine $T_{overtemp}$ from the overheat ratio a . Normally, $T_{overtemp}$ is directly made available by the calibration software.

Table 4-1. Continued.

4	Calculate the working temperature of the sensor, T_w from T_0 and the overtemperature, $T_{overtemp}$.
5	Determine the calibration constants A , B , and n by power-law curve fitting of the calibration data.
6	For actual flow measurements, record the flow temperature, T_{flow} and CTA output voltage, E_{flow}
7	Compute flow velocity u_{flow} from Equation 4-5.

4.1.2 Temperature Measurements

Thermocouples are used to measure the temperatures of the inner and outer Si rings of the heat exchanger device, and that of the hot air exiting the center channel. Faster response time and maximum operating temperature range are the two important considerations for the selection of the thermocouples. Accordingly, K-type thermocouples made of nickel alloys Chromega and Alomega [34] are chosen. Specifically, the unsheathed fine-gage thermocouple of wire diameter 250 μm , CHAL-010, having a response time of 2 seconds and a maximum working temperature of around 800 $^{\circ}\text{C}$ is used for the temperature measurements. The thermocouple outputs are connected to different input channels of a temperature measurement module, USB-TEMP, from Measurement Computing [35]. The measurement module and the thermocouples used are shown

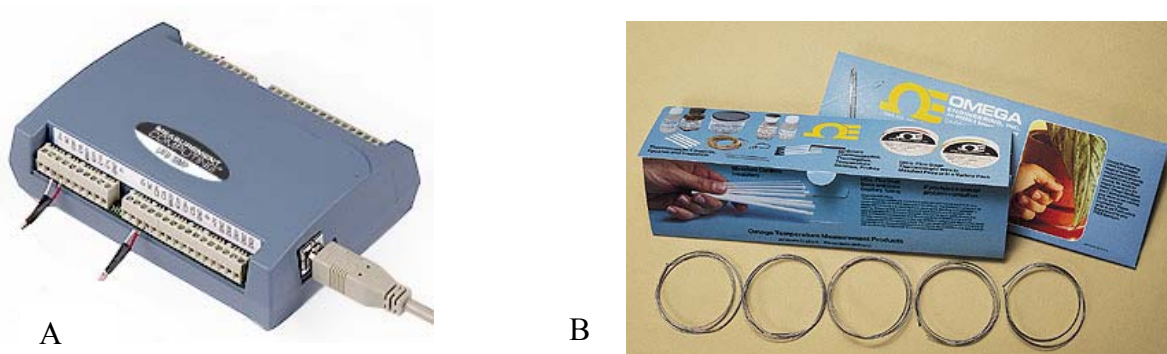


Figure 4-4. Temperature measurement tools. A) Temperature module. [Figure courtesy Measurement Computing] B) Thermocouples, CHAL-010. [Figure courtesy of Omega]

in Figure 4-4. The temperature data from the USB output of the temperature module is recorded in a PC using LabView software and is used later for various analyses.

Outer silicon ring temperatures are measured at three different points around the circumference of the device to get a sense of the temperature profile around the device, especially for the experiments with external cross-flow. Temperature measurements were recorded at the 9'o clock, 12'o clock and 3'o clock positions, as these cover the minimum and maximum temperatures around the circumference of the device. The temperature measurement points and the direction of cross-flow are shown in Figure 4-5. It should be noted that, with ease and accuracy of measurements in mind, the outer ring temperatures are measured on the surface of the outer silicon ring. For the measurement of inner silicon ring temperature, a thermocouple is made to contact the inner ring through the access window designed for this purpose, as described in Section 3.4. Measurement of hot-air temperature is achieved by means of another thermocouple held close to the exit of the center channel of the device. A separate thermocouple is used to measure the ambient temperature. In order to make accurate temperature measurements, all the thermocouples are held stably in place using externally supported clips.

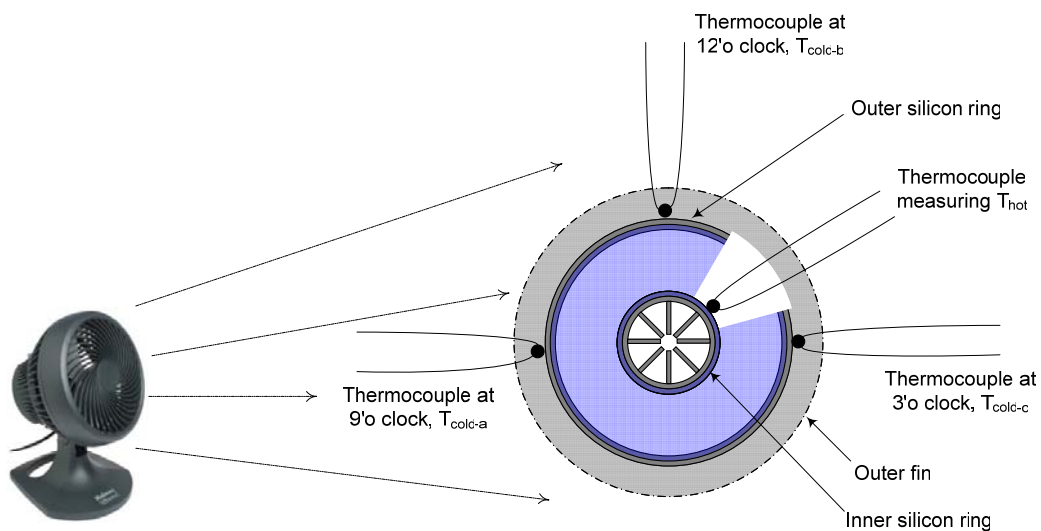


Figure 4-5. Device temperature measurement points.

4.2 Test Matrix and Actual Test Results

A battery of experiments is performed to characterize the heat exchanger device under different temperatures and flow velocities of the hot-air. The heat gun is configured to operate in the variable temperature/variable flow rate mode. In this mode, eight different temperature settings and eight different flow settings, constituting a total of sixty-four combinations are possible. Among these, a set of twenty-four combinations – all of the eight flow settings repeated for three different temperature settings, are chosen. This set of experiments is repeated, in turn, for three different cross-flow conditions (zero cross-flow, and two settings of the miniature fan) making the total number of experiments seventy-two. Table 4-2 makes a list of all the experiments that are performed.

For each experiment, five different steady-state temperatures are measured simultaneously; these temperatures are listed in Table 4-3. In addition to these, a one-time measurement of the ambient temperature, $T_{ambient}$ is also made. Hot-air flow velocities through the center channel ($V_{exhaust-1}$ through $V_{exhaust-8}$), are measured independently with the lowest temperature setting on the heat gun. The flow velocity measurements are not repeated for higher temperature settings as the flow temperature exceeds the operating range of the cross-wire probe. The hot-air flow velocities are assumed to remain the same across the various temperature settings, but this assumption was not explicitly verified. The cross-flow velocity ($V_{cross-flow-1}$, $V_{cross-flow-2}$) measurements are also performed independently.

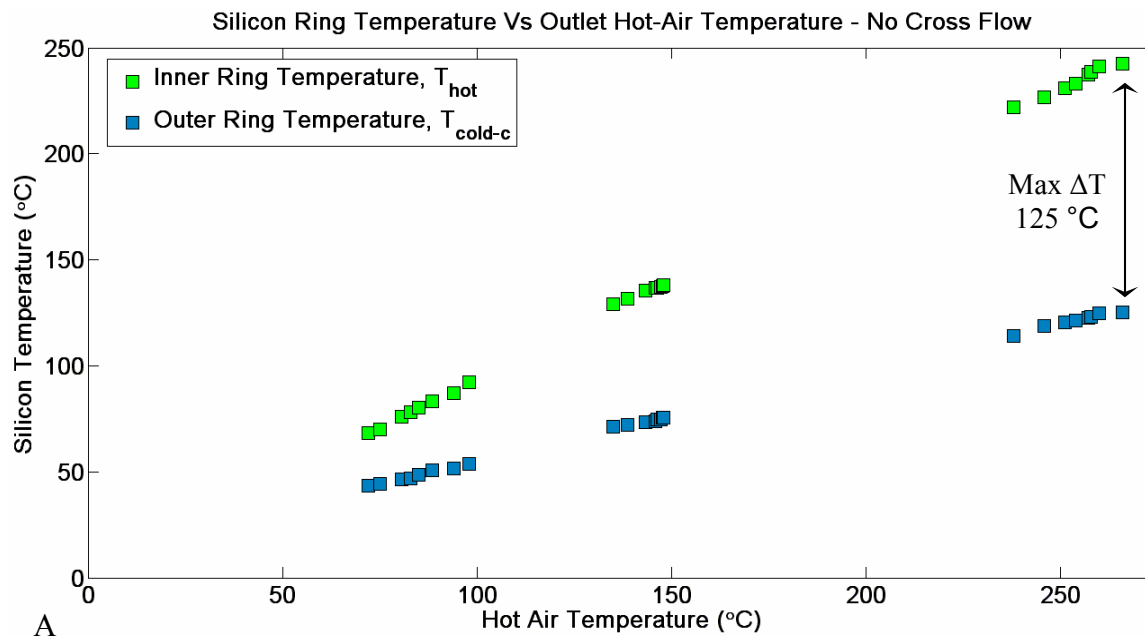
The measured temperature data is analyzed by plotting various graphs. The first set of plots (Figure 4-6) shows the variation in the inner and outer silicon ring temperatures with increasing hot-air temperature.

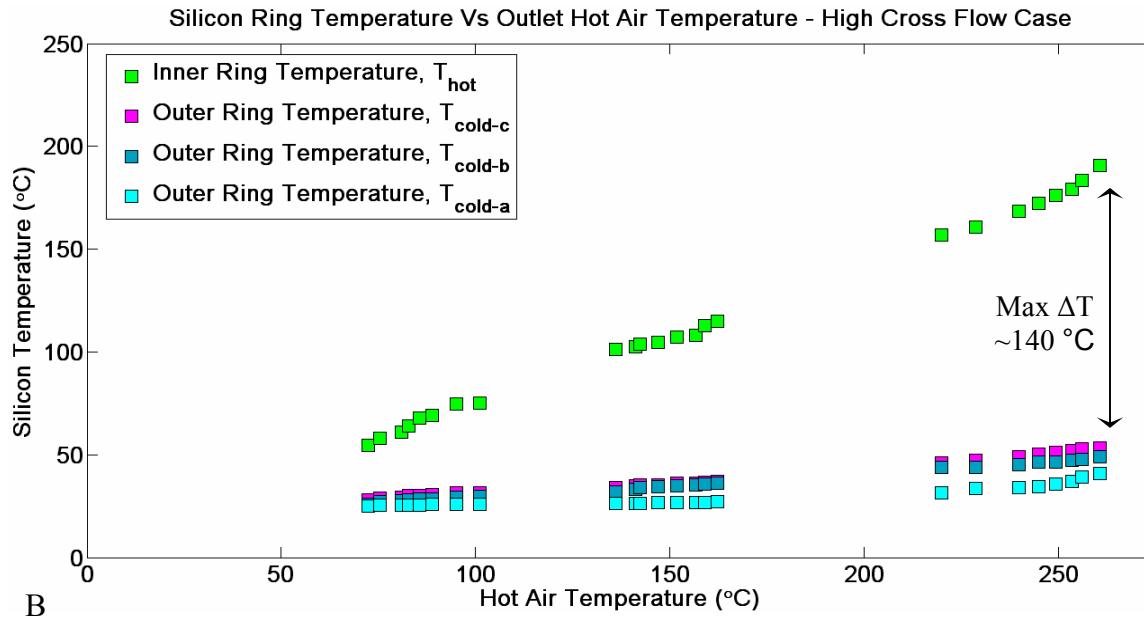
Table 4-2. Heat Exchanger Characterization Matrix.

Set Number	Cross-flow velocity	Hot-air temperature	Hot-air velocity
1	No cross-flow	$T_{exhaust-1}$	$V_{exhaust-1}$ through $V_{exhaust-8}$
		$T_{exhaust-2}$	$V_{exhaust-1}$ through $V_{exhaust-8}$
		$T_{exhaust-3}$	$V_{exhaust-1}$ through $V_{exhaust-8}$
2	$V_{cross-flow-1}$	$T_{exhaust-1}$	$V_{exhaust-1}$ through $V_{exhaust-8}$
		$T_{exhaust-2}$	$V_{exhaust-1}$ through $V_{exhaust-8}$
		$T_{exhaust-3}$	$V_{exhaust-1}$ through $V_{exhaust-8}$
3	$V_{cross-flow-2}$	$T_{exhaust-1}$	$V_{exhaust-1}$ through $V_{exhaust-8}$
		$T_{exhaust-2}$	$V_{exhaust-1}$ through $V_{exhaust-8}$
		$T_{exhaust-3}$	$V_{exhaust-1}$ through $V_{exhaust-8}$

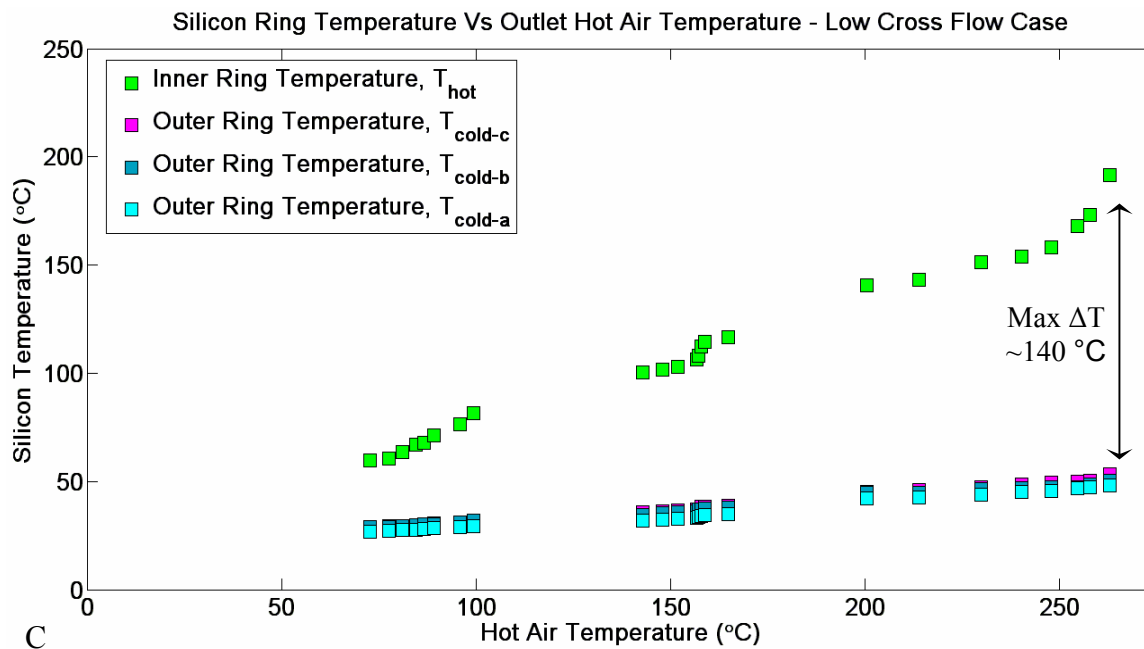
Table 4-3. Temperatures measured during heat exchanger characterization.

Serial Number	Temperature measured
1	Inner silicon ring temperature, T_{hot}
2	Outer silicon ring temperature at 9'o clock position, T_{cold-a}
3	Outer silicon ring temperature at 12'o clock position, T_{cold-b}
4	Outer silicon ring temperature at 3'o clock position, T_{cold-c}
5	Temperature of hot-air exiting the center channel, $T_{exhaust}$





B



C

Figure 4-6. Variation of inner and outer ring temperatures with increasing hot-air temperature. A) No cross-flow case. B) High cross-flow case. C) Low cross-flow case.

Referring to Figure 4-6(A), the zero cross-flow case, a steady increase in both inner and outer ring temperatures with hot-air temperature, $T_{exhaust}$ is noticeable; also, the difference between ring temperatures, $\Delta T = T_{hot} - T_{cold}$ increases linearly with $T_{exhaust}$. In this plot, only one

outer ring temperature data is shown as, without cross-flow, the outer ring temperature around the circumference of the device is found to be fairly uniform. Figures 4-6(B) and (C) show ring temperature variation in the presence of cross-flow. Apparently, a larger temperature differential, ΔT can be observed - without cross-flow cooling, the maximum ΔT achieved is 125 °C, whereas with cross-flow cooling the maximum ΔT achieved is approximately 140 °C. However, no striking improvement in ΔT is observed as the cross-flow velocity is increased from low to high. This is mainly due to the fact that the difference in cross-flow velocities for the low and high cases is only 0.3 m/s. From cross-flow velocity measurements using hot-wire anemometer, $V_{cross-flow-1} = 2.6$ m/s and $V_{cross-flow-2} = 2.9$ m/s.

From the experimentally observed maximum temperature differential, ΔT , best case thermal ratio of the heat exchanger can be calculated. Thermal ratio is a measure of the thermal isolation performance of the heat exchanger, and is defined as the ratio of the temperature difference between the hot and cold sides to the maximum temperature difference possible. It is given by

$$\varepsilon_{thermal} = \frac{\Delta T}{T_{exhaust} - T_{ambient}} = \frac{T_{hot} - T_{cold}}{T_{exhaust} - T_{ambient}} . \quad (4-6)$$

For the radial in-plane heat exchanger characterized here, the thermal ratio is

$$\varepsilon_{thermal} = \frac{T_{hot} - T_{cold}}{T_{exhaust} - T_{ambient}} = \frac{140^{\circ}\text{C}}{250^{\circ}\text{C}} = 0.56 . \quad (4-7)$$

Also, the maximum heat transfer rate, Q , from the hot-air into the heat exchanger can be determined from the measured ring temperature values:

$$Q = \frac{T_{exhaust} - T_{hot}}{\theta_{convh} + \theta_{SiRing}} = 0.144\text{W} . \quad (4-8)$$

This implies that a maximum power of 144 mW is extracted from the hot-air stream. This can be compared with energy transfer rate of the hot-air flow in the center channel of the device. Using thermophysical properties of dry air from standard literature, and assuming slug flow through the center channel, the mass flow rate, $\frac{dm}{dt}$, and hence the energy transfer rate can be calculated as follows:

$$\frac{dm}{dt} = \rho V_{\text{exhaust}} A_{\text{cross-section}} \quad (4-9)$$

where, ρ is the density of air, V_{exhaust} is the hot-air velocity, and $A_{\text{cross-section}}$ is the cross-sectional area of the center exhaust channel. The energy transfer rate of the hot-air flow is given by

$$Q_{\text{hot-air}} = \frac{dm}{dt} C_p \Delta T, \quad (4-10)$$

where, C_p is the specific heat capacity of air. For the flow conditions under which the heat exchanger device is tested, this computes to $Q_{\text{hot-air}} = 58W$, indicating that only a small fraction of the heat energy is extracted from the hot-air stream.

With regard to variation in outer ring temperature around the circumference of the device, the temperature at the 3'o clock position, $T_{\text{cold-c}}$ is found to be the highest followed by $T_{\text{cold-b}}$ and then $T_{\text{cold-a}}$. High outer ring temperature at the 3'o clock position on the device is expected as it is completely hidden from the cross-flow by the heat exchanger device itself. On the other hand, the 9'o clock position shows low temperatures as it receives maximum cross-flow. Moreover, with higher cross-flow velocity, a larger circumferential variation in outer ring temperature can be noticed as a result of increased convection.

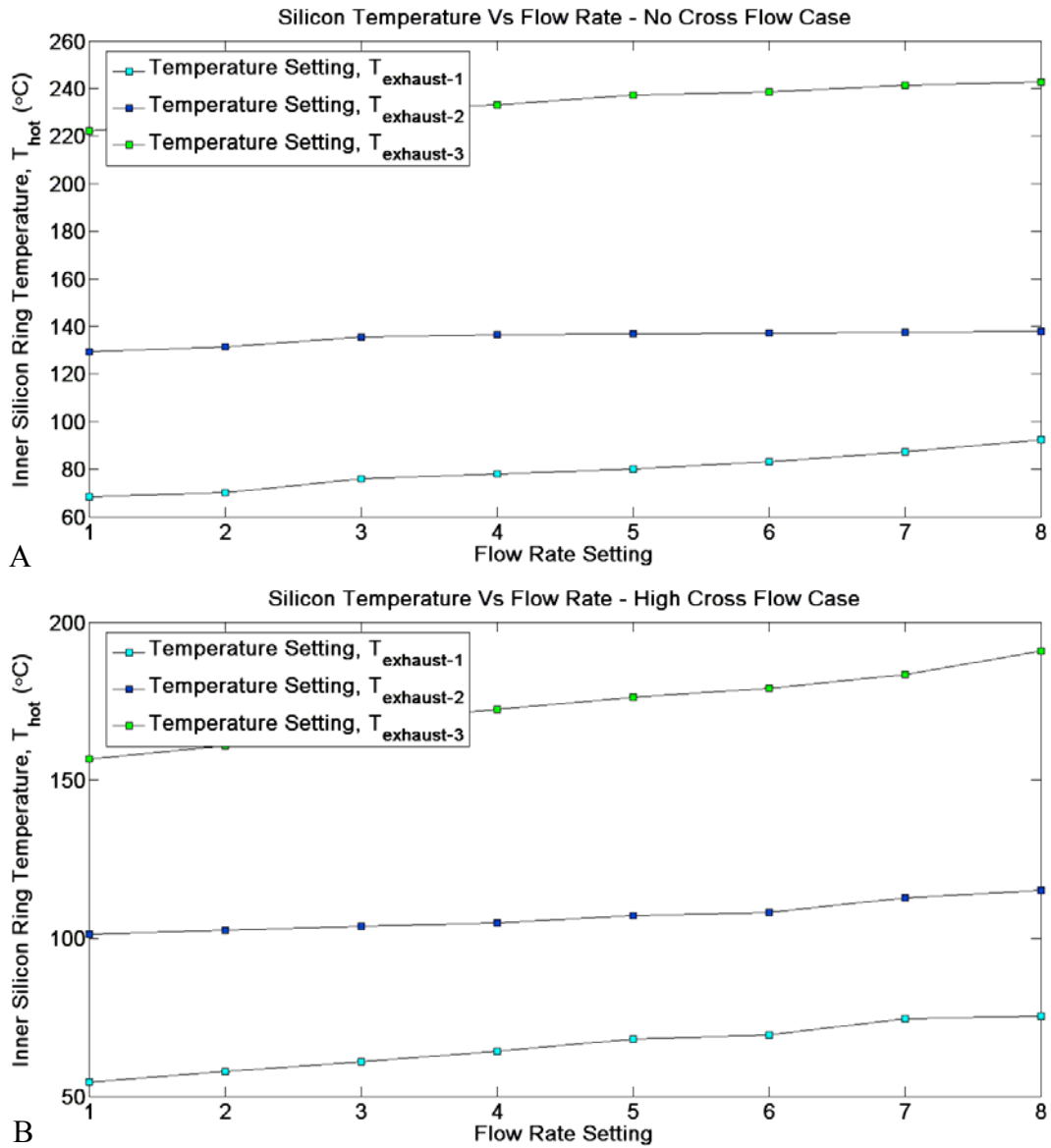


Figure 4-7. Variation in inner silicon ring temperature with hot-air velocity. A) No cross-flow case. B) High cross-flow case. C) Low cross-flow case.

Figure 4-7 shows the variation in inner silicon ring temperature, T_{hot} with increasing hot-air velocity, $V_{exhaust}$ at three different temperatures, $T_{exhaust-1}$ through $T_{exhaust-3}$. Referring to Figure 4-7(A), the zero cross-flow case, it can be seen that there is a small (around 20 °C), but perceptible increase in inner ring temperature as the flow velocity is increased. The same trend is observed for other hot-air temperatures as well, and also in the presence of cross-flow cooling. However, with cross-flow, the curves are shifted down because of external cooling. The main

observation from these plots is that the inner ring temperature increases with increasing hot-air velocity. This is expected because a higher flow velocity generally results in a higher convection heat transfer coefficient, h which implies lower θ_{convh} and larger T_{hot} . Nevertheless, in light of the fact that the hot-air temperature increases slightly with hot-air velocity (due to non-ideal heat gun), it can be inferred that the net increase in ring temperature because of increasing hot-air velocity is small.

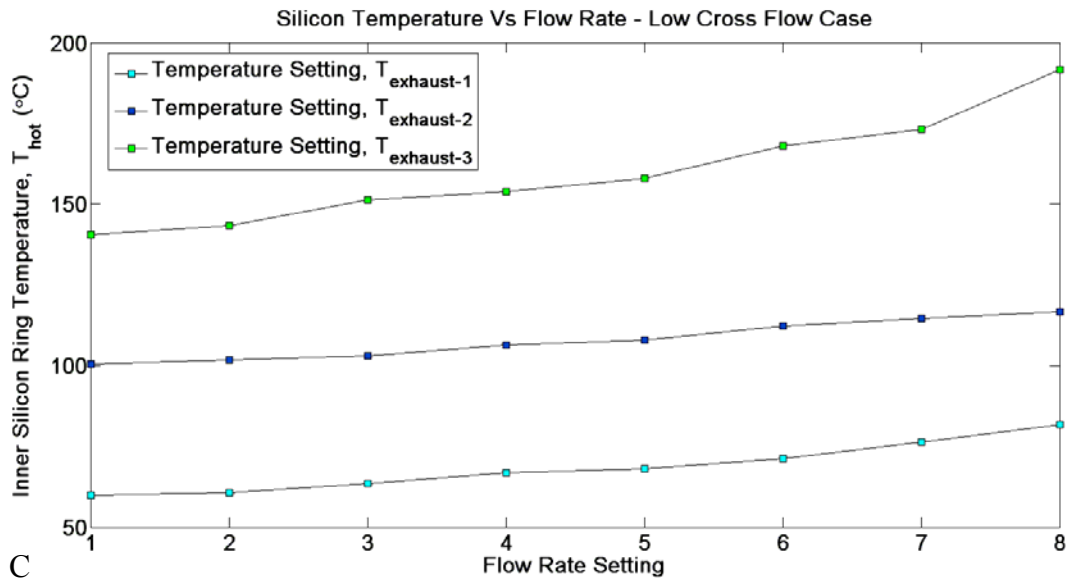


Figure 4-7. Continued.

4.3 Comparison with Predicted Results

The experimental results obtained from heat exchanger characterization described in the previous section are compared with results predicted by the detailed analytical model of the heat exchanger device developed in Section 2.5. Specifically, all the thermal resistances in the equivalent circuit shown in Figure 2-11(A) are computed, using which estimates for the inner and outer silicon ring temperatures are obtained for a range of hot-air temperatures, $T_{exhaust}$, from 0 to 270 °C. The device dimensions, hot-air velocity, $V_{exhaust}$, and cross-flow velocity, $V_{cross-flow}$

are the other input parameters used in this prediction. For calculating thermal conductivity and other fluid properties that are temperature dependent, the measured T_{hot} and T_{cold} are used.

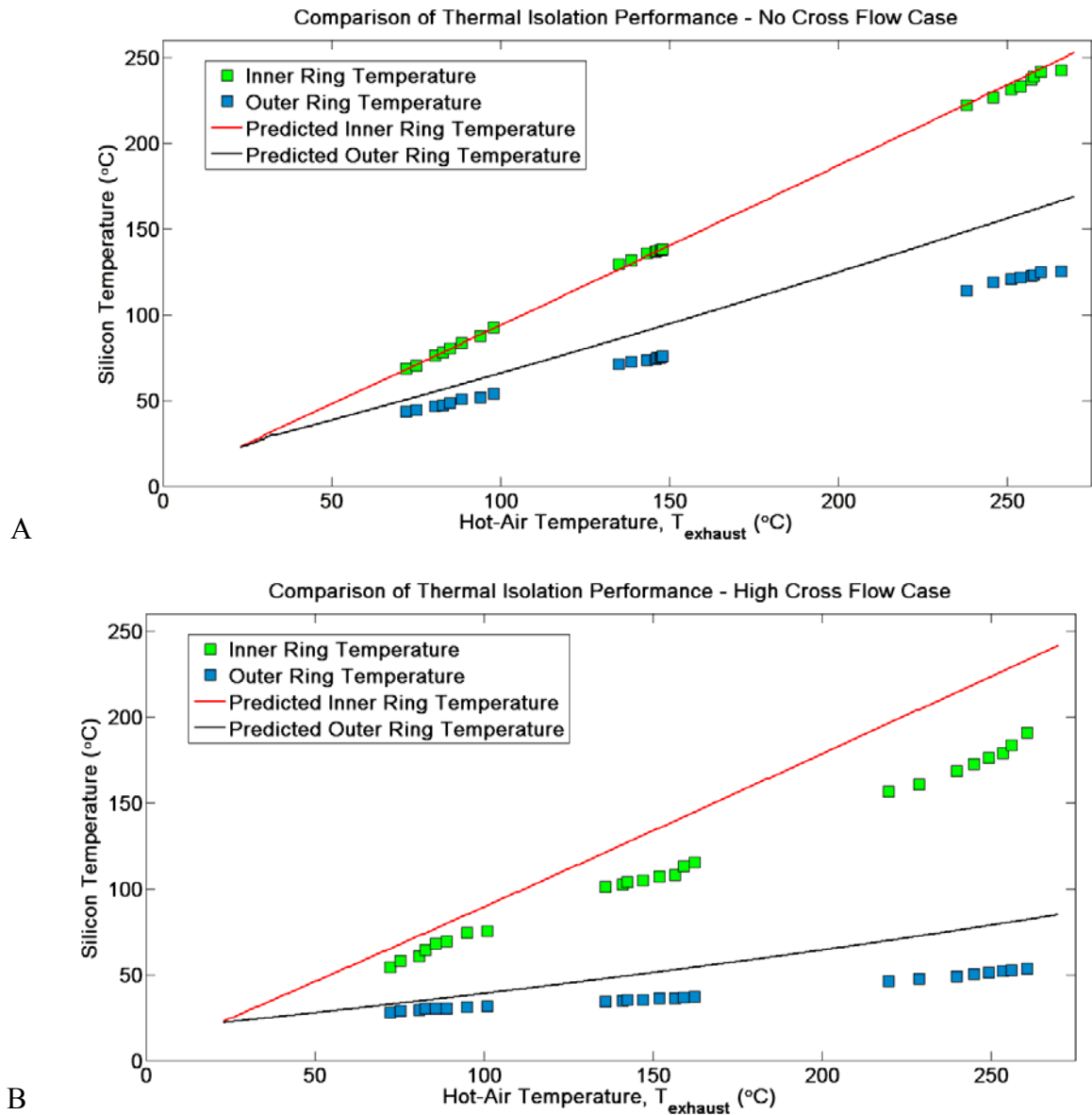


Figure 4-8. Comparison of experimental results with results predicted by analytical model. A) No cross-flow case. B) High cross-flow case. C) Low cross-flow case.

The theoretically estimated results are plotted along with the experimental results for comparison (Figure 4-8). From the plots, it can be seen that the analytical and experimental results match closely for the no cross flow case; however, with non-zero cross-flow velocity, the

experimental results deviate significantly from the theoretical predictions especially for high hot-air temperatures. The maximum deviation of 50 °C is observed for the low cross-flow case.

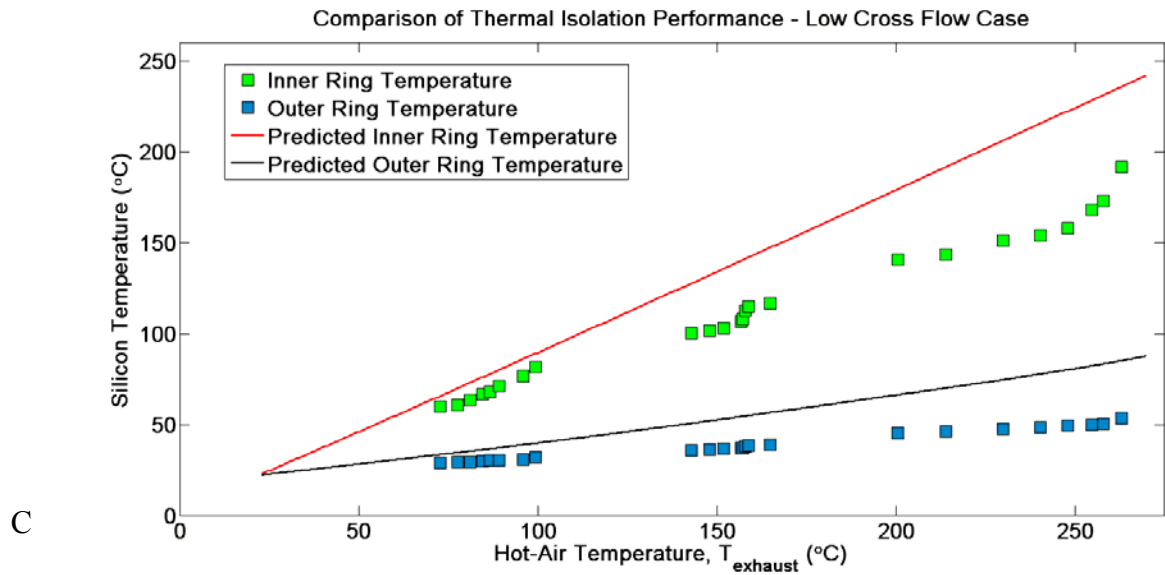


Figure 4-8. Continued.

4.4 Limitations of the Experimental Setup

One main drawback of the measurement strategy employed to characterize the heat exchanger device is the usage of thermocouples to measure the various temperatures. The accuracy of a thermocouple temperature measurement largely depends on the how well the thermocouple is in contact with the surface of interest. Although efforts are made to position and hold the thermocouples in place using external supports, and these connections are monitored periodically during heat exchanger device testing, there still remains a degree of uncertainty related to thermocouple position and orientation especially in the presence of cross-flow.

The next source of error in heat exchanger testing is the heat gun. Ideally, in variable temperature/variable flow rate mode, the temperature of the hot-air is independent of the flow rate setting. However, the hot-air temperature is found to vary by at least 30 °C between the lowest and highest flow rate setting. This makes it difficult to understand how ΔT responds to changes in hot-air flow velocity at a given temperature.

The other limitation of this experimental setup is the fairly large window in the outer silicon ring that is designed to provide access to inner ring for temperature measurement. When the device is tested with cross-flow cooling, a portion of the inner ring gets indirectly exposed the cross-flow resulting in lower inner ring temperature than its true value. This helps account for the disparity between the theoretical prediction and actual experimental results evident in Figures 4-8(B) and 4-8(C).

4.5 Summary

The thermal isolation performance of the radial in-plane heat exchanger device is characterized under different conditions. The experimental results obtained are found to agree well with results from analytical model except for the inner ring temperature in presence of cross-flow. The possible reasons of the deviation are also examined.

CHAPTER 5 CONCLUSIONS AND FUTURE WORK

This chapter recapitulates the key goals and accomplishments of this research work. It also summarizes important results and suggests possible improvements and future work for heat exchanger device design, fabrication and characterization.

5.1 Conclusions

Microscale thermoelectric (TE) power generation has, of late, gained increased attention due to two important reasons: growing demand for portable power in the microwatt to milliwatt range [19], and availability of micromachinable TE materials with improved efficiency [1]. The principal challenge confronting microscale TEG design is to achieve a high temperature differential across thermopile ends that are only hundreds of micrometers apart [20], [21]. The main goal of this research work is to build a heat exchanger platform for a TE microgenerator that converts waste heat from exhaust gas to useful power, while attempting to meet the challenge above.

To this end, the concept of a stacked silicon tubular heat exchanger device was proposed. By design, the stack is made of multiple TE modules, each comprising of an inner and an outer silicon ring connected only by a thin supporting membrane. The structural stability of such a device was, however, questionable. Through actual fabrication of the proposed heat exchanger device using polyimide for the supporting membrane, the idea is proven to be indeed feasible. In the TE modules, the absence of silicon underneath the thermocouples limits thermal leakage to the low conductivity polyimide resulting in high thermal efficiency; whereas, silicon heat fins formed on the inner and outer sides serve to enhance convective heat transfer.

The fabricated heat exchanger device was characterized in the laboratory under different conditions – varying temperatures and flow velocities of the exhaust gas, with and without

external cross-flow cooling. A maximum temperature difference of 140 °C between the inner and the outer rings was achieved for an exhaust gas temperature of around 250 °C, indicating a thermal ratio close to 60 %. An analytical heat transfer model of the device was developed in MATLAB to corroborate experimental results. The model predictions match reasonably well with measured temperatures for the test without cross-flow. There are significant deviations observed in the cross-flow case, but this is attributed to limitations of the experimental setup.

In summary, a micro heat exchanger device for thermoelectric waste heat power generation was designed, fabricated and demonstrated to achieve high thermal efficiency.

5.2 Future Work

Although successful in creating a fairly large temperature differential, the heat exchanger device developed in this research work has its own shortcomings. Firstly, the device does not lend itself to easy temperature measurements (necessary for thermal modeling validation and future device designs). Particularly, measuring inner ring temperature is quite challenging since it is enclosed completely within the outer ring. The second disadvantage is the procedure used to bond the TE modules. While it is true that manual application of epoxy around the silicon rings offers a quick and dirty way to build the stack, it is labor intensive, demands considerable caution, and the method is prone to defects. An inadequate amount of epoxy can cause air gaps, resulting in thermal leakage, whereas an excess of the same could clog the center exhaust gas channel.

Based on these thoughts, future investigations in this research work can be pursued in two areas: a better and more reliable bonding/stacking technique and structural modifications to enable convenient temperature measurements. The following subsections suggest possible options in each area.

5.2.1 Eutectic Bonding of TE Modules

From a bonding perspective, the silicon substrates of the TE modules offer an advantage in that many of the emerging solutions for 3D integration of ICs [36] apply directly to bonding TE modules as well. On these lines, eutectic bonding is an established method used in silicon wafer bonding. The principle here is to use an intermediate bonding material, in this case a eutectic alloy from two or more metals. A eutectic alloy combination offers a combined melting point that is much lower than the individual melting points of the constituent elements, enabling relatively low-temperature bonding. Common eutectic pairs found in the literature include copper-tin, gold-tin, gold-silicon and gold-indium.

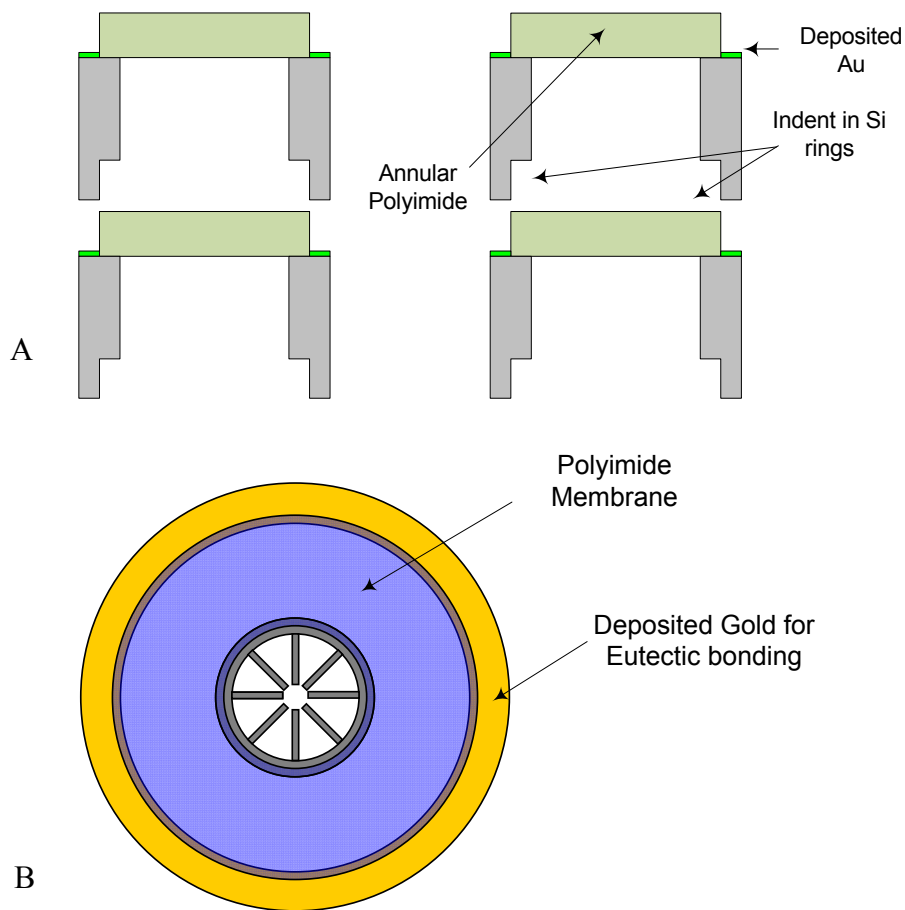


Figure 5-1. Eutectic bonding of TE modules. A) Cross-section of TE modules with deposited Au. B) Top view of TE module with deposited Au.

The obvious choice for bonding of heat exchanger modules is Au-Si. Previous implementations [37], [38] of Au-Si eutectic bonding report an alloy formation temperature of less than 400 °C, well within the operating temperature range of polyimide. The only additional process steps necessary for eutectic bonding of TE modules are deposition of chromium (for adhesion) and gold on the front-side and nested DRIE on the back-side to realize a cross-section (Figure 5-1(A)). Once the TE modules are fabricated and stacked, bonding of the entire stack can be achieved in a single instance by heating to the eutectic temperature. The primary challenge here would be to ensure electrical insulation between the thermoelectric devices and the conductive bonding layer.

5.2.2 Integrated Temperature Measurement

Integrated temperature measurement using resistance temperature detectors (RTDs) present a promising alternative to the use of externally applied thermocouples. RTDs respond to a change in temperature with a change in resistance; the amount of resistance change for a given temperature change is dependent on a material property called the temperature coefficient of resistance (TCR). Resistance of any material is given by

$$R(T) = R(T_0) [1 + \alpha(T - T_0)] \quad (5-1)$$

where $R(T)$ is the resistance at temperature T , $R(T_0)$ is the resistance at reference temperature T_0 , and α is the temperature coefficient of resistance of the material. Usually, materials with high TCR such as platinum and nickel form good RTDs.

RTDs can easily be integrated into the heat exchanger modules by incorporating additional process steps for metal deposition and patterning prior to polyimide patterning. RTDs can be added to the inner and outer silicon rings (Figure 5-2). There may be some loss of thermal efficiency because of leakage through the RTD; but this can be minimized by careful design.

The real challenge, however, lies in performing the back-side DRIE without destroying the metal resistors that may only be a few hundred nanometers thick.

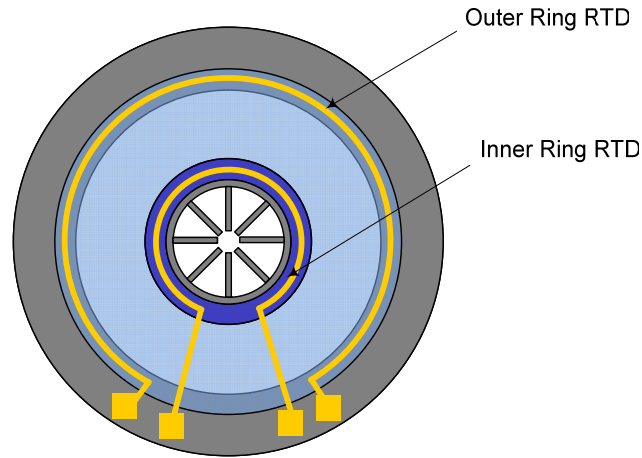


Figure 5-2. Top view of the TE module with integrated RTDs.

As final part of this research, attempts are made to implement platinum RTDs on the large 13 mm heat exchanger modules. A seed layer of chromium is first deposited to provide good adhesion to silicon substrate, followed by deposition of the platinum RTD and a very thin gold layer to enable easy wire bonding to RTD pads. Consecutively, the regular process steps for heat exchanger module fabrication are performed. After fabrication, it is observed that the inner ring RTDs of all the modules invariably fail continuity test. Careful scrutiny reveals fracturing of the RTDs mostly in the region between silicon rings where the RTD is supported only by the polyimide membrane on top. Although, the failure mechanism is not thoroughly understood at this point in time, cracks formed in the polyimide due to high film stress developed during DRIE are speculated as a possible reason. This subject therefore offers a worthy subject for future examination.

In conclusion, although the stacked radial heat exchanger platform is designed to specifically for thermoelectric power generation, the scope of the principles and fabrication methods developed reach out to several other applications requiring high thermal isolation such

as thermoelectric cooling, micro reactors and the like [23], [39]. With MEMS technology making new strides by the day, an extension of the concepts developed in this research may lead to ground-breaking new innovations.

LIST OF REFERENCES

- [1] R. Venkatasubramanian, E. Siivola, T. Colpitts, and B. O'Quinn, "Thin-film thermoelectric devices with high room-temperature figures of merit," *Nature*, vol. 413, no. 6856, pp. 597-602, 2001.
- [2] Wikipedia. (2008, Jul.). Radiator [Online], Available: <http://www.wikipedia.org/wiki/Radiator>
- [3] S. Kakaç and H. Liu, *Heat Exchangers – Selection, Rating and Thermal Design*. Boca Raton, FL: CRC Press, 2002.
- [4] Alibaba.com. NP Skived Fin Heat Sink [Online], Available: http://npowertek.trustpass.alibaba.com/product/11645462/NP_Skived_Fin_Heat_Sink.html
- [5] D. B. Tuckerman and R. F. W. Pease, "High-performance heat sinking for VLSI," *IEEE Electron Device Lett.*, vol. EDL-2, no. 5, pp. 126-129, May 1981.
- [6] D. T. Crane and G. S. Jackson, "Optimization of cross flow heat exchangers for thermoelectric waste heat recovery," *Energy Conversion and Management*, vol. 45, pp. 1565-1582, 2004.
- [7] F. P. Incropera and D. P. DeWitt, *Fundamentals of Heat and Mass Transfer*, 5th ed., Hoboken, NJ: John Wiley & Sons Inc., 2002.
- [8] D. Munding, R. Beach, W. Benett, R. Solarz, W. Krupke, R. Staver, and D. Tuckerman, "Demonstration of high performance silicon microchannel heat exchangers for laser diode array cooling," *Appl. Phys. Lett.*, vol. 53, pp. 1030-1032, 1988.
- [9] J. Arthur, W. H. Tompkins, C. Troxel, Jr., R. J. Contolini, E. Schmitt, D. H. Bilderback, C. Henderson, J. White, and T. Settersten, "Microchannel water cooling of silicon X-ray monochromator crystals," *Rev. Sci. Instrum.*, vol. 63, pp. 433-436, 1992.
- [10] S. Wu, J. Mai, Y. C. Tai, and C. M. Ho, "Micro heat exchanger by using MEMS impinging jets," in *Proc. IEEE Micro Electro Mechanical Systems*, 1999, pp. 171-176.
- [11] C. H. Amon, J. Murthy, S. C. Yao, S. Narumanchi, C. F. Wu, and C. C. Hsieh, "MEMS-enabled thermal management of high-heat-flux devices EDIFICE: embedded droplet impingement for integrated cooling of electronics," *Experimental Thermal and Fluid Science*, vol. 25, pp. 231-242, 2001.
- [12] M. J. Ellsworth, Jr. and R. E. Simons, "High powered chip cooling - air and beyond," *Electronics Cooling*, vol. 11, no. 3, pp. 14-22, Aug. 2005.

- [13] L. G. Fréchet, C. Lee, S. Arslan, Y.-C. Liu, “Design of a microfabricated rankine cycle steam turbine for power generation,” in *Proc. ASME International Mechanical Engineering Congress*, Washington, DC, Nov. 15-21, 2003, pp. 335–344.
- [14] S. Sullivan, X. Zhang, A. A. Ayon, J. G. Brisson, “Demonstration of a microscale heat exchanger for a silicon micro gas turbine engine,” in *Proc. 11th International Conf. Solid-State Sensors, Actuators and Microsyst. (Transducers’01)*, Munich, Germany, Jun. 2001, pp. 1606–1609.
- [15] L. Sitzki, K. Borer, E. Schuster, P.D. Ronney, and S. Wussow, “Combustion in microscale heat-recirculating burners,” in *Proc. Third Asia-Pacific Conference on Combustion*, Seoul, Korea, Jun. 24-27, 2001, pp. 473–476.
- [16] A. Cohen, “Microcombustor and Combustion-based Thermoelectric Microgenerator,” U.S. Patent 6 613 972, Sep. 2, 2003.
- [17] S. B. Schaevitz, A MEMS Thermoelectric Generator. Cambridge, MA, Massachusetts Institute of Technology, 2000, Ph.D.
- [18] Thin Film Peltier Cooler, MPC-D901 Datasheet [Online], Available: www.micropelt.com.
- [19] S. A. Jacobson and A. H. Epstein, “An informal survey of power MEMS,” in *Proc. Int. Symp. Micro-Mechanical Engineering*, Tsuchiura and Tsukuba, Japan, Dec. 1–3, 2003, pp. 513–520.
- [20] S. B. Schaevitz, A. J. Franz, K. F. Jensen, and M. A. Schmidt, “A combustion-based MEMS thermoelectric power generator,” in *Proc. 11th International Conf. Solid-State Sensors, Actuators and Microsyst. (Transducers’01)*, Munich, Germany, Jun. 2001, pp. 30-33.
- [21] M. Strasser, R. Aigner, M. Franosch, G. Wachutka, “Miniaturized thermoelectric generators based on poly-Si and poly-SiGe surface micromachining,” in *Proc. 11th International Conf. Solid-State Sensors, Actuators and Microsyst. (Transducers’01)*, Munich, Germany, Jun. 2001, pp. 535-542.
- [22] G. Min, D. M. Rowe, and F. Volklein, “Integrated thin film thermoelectric cooler,” *Electronics Letters*, vol. 34, no. 2, pp. 222-223, 1998.
- [23] A. Gross, H. Baoling, G.-S. Hwang, C. Lawrence, N. Ghafouri, S. W. Lee, H. Kim, C. Uher, M. Kaviani, K. Najafi, “A multistage in-plane micro-thermoelectric cooler,” in *Proc. 21st IEEE Int. Conf. MEMS*, Tucson, AZ, Jan. 13-17, 2008, pp. 840-843.
- [24] D.-Y. Yao, C.-J. Kim, and G. Chen, “Design of thin-film thermoelectric microcoolers,” in *Proc. ASME International Mechanical Engineering Congress & Exposition*, Orlando, FL, Nov. 5-10, 2000.

- [25] I. Boniche, C.D. Meyer, P.J. Taylor, N.K. Dhar, D.P. Arnold, “Progress towards a micromachined thermoelectric generator using PbTe and PbSnSeTe films,” in *Tech. Dig. 6th Int. Workshop Micro Nanotechnology for Power Generation and Energy Conversion Apps. (PowerMEMS 2006)*, Berkeley, CA, Nov. 2006, pp. 195-198.
- [26] I. Boniche, B. C. Morgan, P. J. Taylor, C. D. Meyer, and D. P. Arnold, “Process development and material characterization of polycrystalline Bi₂Te₃, PbTe, and PbSnSeTe thin films on silicon for MEMS thermoelectric generators,” *J. Vacuum Sci. Tech. A*, (in press), Jul./Aug. 2008.
- [27] W. M. Rohsenow, J. P. Hartnett, and Y. I. Cho, *Handbook of Heat Transfer*, 3rd Ed., New York, NY: McGraw Hill, 1998.
- [28] R. L. Webb, *Principles of Enhanced Heat Transfer*, New York, NY: John Wiley & Sons Inc., 1994.
- [29] M. A. Douglas, “Trench etch process for a single-wafer RIE dry etch reactor,” U.S. Patent 4 855 017, Aug. 8, 1989.
- [30] S. D. Senturia, *Microsystem Design*, New York, NY: Springer Science & Business Media Inc., 2001.
- [31] HD Microsystems, HD-8820 Aqueous Positive Polyimide Process Guide [Online], Available: <http://www.hdmicrosystems.com>
- [32] Master Appliances Product Catalog [Online], Available: www.masterappliance.com/Master_Appliance_50th_Catalog.pdf
- [33] F. E. Jorgensen, *How to measure turbulence with hot-wire anemometers – a practical guide*, Skovlunde, Denmark: Dantek Dynamics, 2002.
- [34] Thermoelectric Alloy Property Data [Online], Available: <http://www.omega.com/temperature/z/pdf/z049-050.pdf>
- [35] Specifications – USB-TEMP [Online], Available: www.measurementcomputing.com/pdfs/usb-temp.pdf
- [36] P. Garrou, “Future ICs go vertical”, *Semiconductor International*, Feb. 2005.
- [37] R. F. Wolfenbuttel, “Low-temperature intermediate Au-Si wafer bonding: eutectic or silicide bond,” *Sensors and Actuators A-Physical*, vol. 62, pp. 680-686, 1997.
- [38] D.-J. Yao, G. Chen, C.-J. Kim, “Low temperature eutectic bonding for in-plane type micro thermoelectric cooler”, in *Proc. ASME International Mechanical Engineering Congress and Exposition*, New York, NY, Nov. 11-16, 2001.

- [39] A. Kasuga, S. Tanaka, and M. Eshashi, "Vacuum-packaged micro fuel reformer for high thermal efficiency and low package temperature," in *Proc. 21st IEEE Int. Conf. MEMS*, Tucson, AZ, Jan. 13-17, 2008, pp. 968-971.

BIOGRAPHICAL SKETCH

Sivaraman Masilamani was born in Edaiyur, a small village in Thiruvarur district of Tamilnadu, India. He received his bachelor's degree in electronics and communication engineering from College of Engineering, Anna University, Chennai in the year 2001. Subsequently, he joined Alliance Semiconductor, Bangalore as a IC Design Engineer, designing analog and digital subcircuits for SRAMs and power management ICs.

He started his graduate study in August 2005 at University of Florida, Gainesville. He joined the Interdisciplinary Microsystems Group under the supervision of Dr. David Arnold, focusing his research in the area of microsystems and microfabrication. He also gained industry experience in analog circuit design through internships at Qualcomm, San Diego and Texas Instruments, Melbourne. He received his Master of Science degree in electrical and computer engineering from University of Florida in August 2008. He has since accepted an Analog IC Design Engineer position at Intel, Oregon.

His research interests include analog circuit design for power management ICs, power MEMS, and circuit design for MEMS.